Master Thesis

Condition Monitoring of Flexible Pipe Connectors in Parabolic Trough Solar Collectors

Felix Pander

Examiner: Prof. Dr. Alexander Reiterer

Second Examiner: Prof. Dr. Stefan Glunz

Advisers: Dr.-Ing. Sonja Kallio

In cooperation with the German Aerospace Center, Almeria (DLR)

Albert-Ludwigs-University Freiburg
Faculty of Engineering
INATECH

July 2025

Declaration

I hereby declare, that I am the sole author and composer of my thesis and that no other					
sources or learning aids, other than those listed, have been used. Furthermore, I declare					
that I have acknowledged the work of others by providing detailed references of said work.					
I also hereby declare that my thesis has not been prepared for another examination or					
assignment, either in its entirety or excerpts thereof.					
Place, Date Signature					

Abstract

Parabolic Trough Collectors are the most commonly used type of Concentrating Solar Power technology, providing renewable energy. They concentrate solar radiation onto a receiver tube, from which heat is transported via a Heat Transfer Fluid to a turbine generating electricity. At the ends of the collectors, flexible pipe connectors accommodate the rotational sun-tracking movement and thermal expansion of materials. Methods for condition monitoring of these connectors are currently under research to enable preventive maintenance.

Several sensors monitor Ball Joint Assemblies at a test rig during accelerated lifetime experiments. In this study, three cameras and a laser sensor are implemented to detect geometrical transformations of the connectors. Additionally, a gas concentration sensor setup measures leakage of evaporated Heat Transfer Fluid from the ball joints. The cycling phase of the experiment comprises 2,700 cycles, representing approximately seven years of plant operation.

Throughout the cycling, no trend of geometric transformation is observed. The angle between the connector tubes varies from cycle to cycle around 1.5°, with an estimated accuracy of 0.5°. Gas concentration measured near one of the ball joints remains low, between 0 ppb to 4 ppb. However, during heat-up of the test rig and at low ambient temperatures, higher gas concentrations of 36.5 ppb and above are observed. The implemented methods did not indicate a need for maintenance, however, observed outgassing after movement stopped suggests that maintenance was necessary. Nonetheless, it remains unclear whether a complete failure could have been anticipated.

List of Abbreviations

2D Two-dimensional

3D Three-dimensional

BJA Ball Joint Assembly

CCS Camera Coordinate System

CIEMAT Centro de Investigaciones Energéticas, Medioambientales y Tecnológicas

CSP Concentrating Solar Power

DLR Deutsches Zentrum für Luft- und Raumfahrt (German Aerospace Center)

HTF Heat Transfer Fluid

PnP Perspective-n-Point

PSA Plataforma Solar de Almeria

PTC Parabolic Trough Collector

RCS Reference Coordinate System

REPA Rotation and Expansion Performing Assembly

RFHA Rotary Flex Hose Assembly

SCADA Supervisory Control and Data Acquisition

Contents

1	Intro	oductio	n	1
2	Fun	dament	tals and State of the Art	4
	2.1	Conce	ntrating Solar Power	4
		2.1.1	Point receiver CSP	4
		2.1.2	Line receiver CSP	5
		2.1.3	Tracking	6
		2.1.4	Heat Transfer Fluid	6
		2.1.5	Rotation and Expansion Performing Assemblies	8
	2.2	REPA	test rig	9
	2.3	Camer	as for visual observation	10
		2.3.1	Camera calibration	11
		2.3.2	Pose estimation	12
		2.3.3	ArUco marker detection	12
	2.4	Laser	distance measurement	14
	2.5	HTF l	eakage measurement	14
		2.5.1	HTF gas detection	14
		2.5.2	Gas concentration sensor Sens-It	15
		2.5.3	HTF leakage measurement system	15
3	Ехр	eriment	tal Setup	17
	3.1	Geome	etric transformation observation	17
		3.1.1	Cameras	17

Contents

		3.1.2	Laser distance sensor	. 1	9
	3.2	HTF 1	leakage sensor	. 2	0
4	Met	hodolo	gy	2	1
	4.1	Experi	iment phases	. 2	1
		4.1.1	Heat-up phase	. 2	1
		4.1.2	Cycling phase	. 2	2
		4.1.3	Maintenance phase	. 2	3
		4.1.4	Second experiment phase	. 2	4
	4.2	Data e	evaluation	. 2	4
		4.2.1	Cameras	. 2	4
		4.2.2	Laser distance sensor	. 2	7
		4.2.3	HTF leakage sensor	. 2	7
5	Resu	ults		2	8
	5.1	Geome	etric transformation observation	. 2	8
		5.1.1	Image analysis	. 2	8
		5.1.2	Laser data analysis	. 3	6
	5.2	HTF 1	leakage sensor measurements	. 3	8
		5.2.1	HTF leakage time series	. 3	8
		5.2.2	HTF leakage analysis	. 4	1
6	Disc	ussion		4	3
	6.1	Measu	arement setup and results	. 4	3
		6.1.1	Cameras	. 4	3
		6.1.2	Laser distance sensor	. 4	6
		6.1.3	Camera and laser combined	. 4	7
		6.1.4	Further ideas for observation	. 4	8
		6.1.5	HTF leakage sensor	. 4	8
		6.1.6	Improved setup ideas	. 5	0
		6.1.7	Combining results from the methods	. 5	1

Contents

	6.2	Use in a CSP Plant	 52
7	Sum	nmary and Outlook	53
Bi	bliogi	raphy	55

List of Figures

1	Series of PTCs each with parabolic-shaped mirror, mounting structure,	
	and receiver tube. The REPA connecting the tube to the field pipes is	
	$marked. \dots \dots$	2
2	The test rig at PSA. It simulates the effects of expansion and rotation of	
	a PTC receiver tube on two REPAs	3
3	Schematic representation of the four main CSP technologies: 1) Parabolic	
	Trough Collector, 2) Solar Tower, 3) Linear Fresnel Reflector, and 4)	
	Parabolic Dish System [5]	5
4	Ball joint assembly for PTCs. Three ball joints (blue circled) are connected	
	by two tubes (yellow dotted, here with insulation)	8
5	Sketch of the REPA test rig with two flex hose REPAs. For this experi-	
	ment, they were replaced by ball joint assemblies [10]	9
6	Pinhole camera model projecting a 3D scene onto a 2D plane [14]	11
7	Exemplary ArUco markers with ID 0 (left) and ID 5 (right) [18]	13
8	Ratio of cylinder concentration (containing a mixture of VP-1, N_2 , and	
	${\rm O}_2)$ and the measured value of the Sens-It sensor [20]	16
9	Setup of three cameras (cyan circles) and reference ArUco markers (orange	
	squares) at the test rig. The tubes of the east and west REPA (purple	
	ovals) are equipped with ArUco markers	18

List of Figures

10	Schematic of the two REPAs (blue) with one target at each lower tube	
	(gray). The test rig is rotating around the green dashed-marked axis.	
	The targets cross the laser beam (red, the dashed part is the imaginary	
	continuation of the beam)	19
11	HTF leakage sensor installed at the test rig with the entrance of the pipe	
	near one ball joint (here shown without its insulation)	20
12	Temperature and pressure of the HTF during the heat-up phase. Heating	
	is carried out in several steps to allow temperature stabilization	22
13	Exemplary snippet of the cycling phase of the REPA test rig. The rota-	
	tional and translational movements follow a fixed pattern throughout the	
	cycling phase, simulating real-world movements in a PTC	23
14	Exemplary image of camera A with the detected markers and their unique	
	IDs. Here, not all markers were detected along the lower tube	25
15	Exemplary view of camera B with the detected markers and their unique	
	IDs. Four markers on the rotating structure form the RCS (yellow). The	
	positions of the markers on the tubes are given with respect to its origin	
	(orange)	26
16	Influence of corner pixel shifts on 3D position for a fixed marker. Bars	
	show the occurrence count of each cumulative pixel shift	29
17	Sensitivity of 3D displacement to pixel shift for all markers	30
18	Exemplary estimated position of the markers observed by camera B with	
	the CCS and the RCS	31
19	Marker positions and line fits based on all detected markers and on the	
	three markers closest to the initial line for the upper tube	33
20	Tube angle difference resulting from excluding the farthest outlying marker	
	position	34
21	Angles over completed cycles at a test rig rotation angle of 90° descending.	
	Filtered data points are indicated by gray dashed lines	35

List of Figures

22	Distance to the eastern REPA target's edges over 40 cycles. The yellow-	
	highlighted cycles indicate when the translation angle of the test rig was	
	moved, after which it was held constant	37
23	Measurement data over the whole experiment, the cycling phase is marked.	38
24	Gas concentration, airflow speed, and HTF temperature over time. The	
	concentration and flow speed are reaching the sensors maximum values	
	during and after heating	39
25	Gas concentration and airflow speed over time during the test rig cycling	
	phase. The concentration remains low throughout	40
26	Gas concentration and ambient temperature over time at low HTF tem-	
	perature, the test rig being stopped. The concentration is increasing every	
	night, when the ambient temperature is lower	40
27	Correlation of experiment values on gas concentration, segmented by phase.	
	The standard deviation (std) of concentration values is given	41
28	Gas concentration against ambient temperature for HTF colder than 70 $^{\circ}\mathrm{C}.$	42
29	Gas concentration against HTF temperature change in three hours for	
	HTF above 70 °C and no cycling	42

List of Tables

1	Characteristics of HTFs at ambient temperature in CSP applications [6][9]	7
2	Maximum and average marker distance to the two line fits. One is based	
	on all markers, the other on the closest three markers to the initial fit. $$.	33
3	Tube angle statistics: mean, standard deviation (std), minimum, maxi-	
	mum, and linear fit slope over cycles	36

1 Introduction

Concentrating Solar Power (CSP) plants convert solar radiation into heat, which can then be used to drive a turbine to generate electricity or as process heat. Mirrors reflect and focus solar rays onto a receiver, where the energy is absorbed and transferred to a Heat Transfer Fluid (HTF). Heat storage systems using molten salts as storage medium allow operation of the electricity production during nighttime and cloudy weather. Therefore, CSP can support the stable operation of electrical grids and supply renewable energy.

Parabolic Trough Collectors (PTCs) are the most commonly used setup in commercial operational plants [1]. A PTC is composed of a mounting structure, a parabolic-shaped mirror, and a receiver tube. The mirror concentrates solar rays on the tube through which the HTF is pumped. Operating conditions of the HTF typically reach up to 400 °C and pressures up to 35 bar. Multiple collectors are connected in series before the HTF enters the field piping system leading to the turbine. The collectors track the sun throughout the day by rotation [2].

The connector between a PTC and the field pipe is called a Rotation and Expansion Performing Assembly (REPA). It has to accommodate rotational tracking and translational movements. The latter is caused by thermal expansion and contraction of the receiver tube material due to day-night temperature differences. Figure 1 shows a series of PTCs with an insulated REPA at the junction connecting to the field pipes.

REPAs are crucial components in PTC systems, where commercial plants in operation report the greatest maintenance effort. They are under high mechanical stress due to the

1 Introduction



Figure 1: Series of PTCs each with parabolic-shaped mirror, mounting structure, and receiver tube. The REPA connecting the tube to the field pipes is marked.

movements, heat, and pressure inside the pipes. Failures can lead to leakages of HTF and further to environmental contamination, downtime of the power plants, and danger of fires. It is therefore advantageous to monitor the condition of the REPAs to foresee potential issues and perform preventive maintenance before a failure of the components occurs.

The German Aerospace Center (Deutsches Zentrum für Luft- und Raumfahrt, DLR) collaborates with the Spanish Centro de Investigaciones Energéticas, Medioambientales y Tecnológicas (CIEMAT), owner of the Plataforma Solar de Almeria (PSA). This research institute, located in the desert of Tabernas with high yearly solar irradiation, offers a variety of experimental setups for the ongoing research on CSP and its different components, materials, and applications [3].

The PSA offers a test rig for accelerated lifetime experiments of REPAs, shown in Figure 2. It includes two REPAs connected in a closed loop through pipes. Heating elements and a pump are integrated into this loop, allowing the HTF to circulate at up to 393 °C and 35 bar. A hydraulic unit applies both rotational and translational motion to the traverse containing the receiver tube, simulating the movements in a solar field. This setup enables accelerated lifetime testing, achieving the equivalent of approximately 30 years of operation in three weeks, corresponding to around 10,000 cycles.

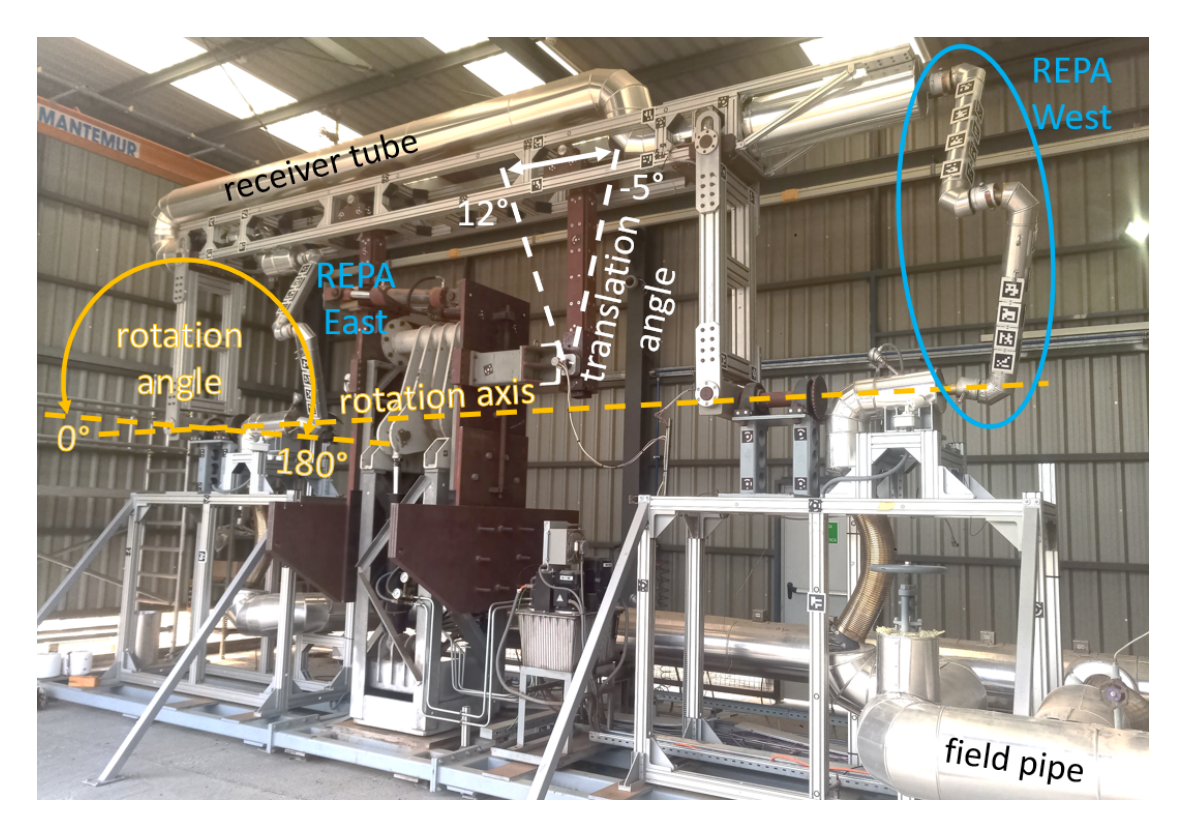


Figure 2: The test rig at PSA. It simulates the effects of expansion and rotation of a PTC receiver tube on two REPAs.

This work is part of the BMWK REPA-3S project, funded by the German Federal Ministry for Economic Affairs and Energy. It integrates three cameras and a laser distance sensor into the test rig to observe for geometrical transformations of the REPAs during cycling. Additionally, a gas detection sensor is installed to measure HTF leakages. These approaches are evaluated for their suitability in condition monitoring based on data collected throughout the experiment.

The fundamentals of CSP, the REPA test rig, and the applied measurement methods are presented in Chapter 2. Chapter 3 describes the installation and configuration of the cameras, laser, and HTF leakage sensor on the test rig. The methodology for the experimental phases and the data evaluation approach are outlined in Chapter 4. Experimental results are presented in Chapter 5 and discussed in Chapter 6. Finally, Chapter 7 provides a summary of the findings and conclusions.

2 Fundamentals and State of the Art

This chapter provides an overview of CSP technology and its applications. It also describes the setup of the REPA test rig at the PSA. Furthermore, it covers the fundamentals of using cameras for structural monitoring, laser distance sensors, and methods for measuring HTF leakages in CSP plants.

2.1 Concentrating Solar Power

CSP systems convert solar radiation into thermal energy, which can be used to drive a turbine for electricity generation. Mirrors reflect and focus solar rays onto a receiver, where the energy is absorbed and transferred to a HTF. It is transported to the turbine through collector pipes. Alternatively, other configurations utilize the thermal energy directly as process heat for industrial need or cooking. Different types of CSP exist, the four most common setups are shown in Figure 3. They are mainly distinguished by the form of the receiver, classified in point and line receivers [4].

2.1.1 Point receiver CSP

In point receiver setups, solar radiation is concentrated onto a single point or plane. This approach is used in Solar Towers and Parabolic Dish Systems. In Solar Towers, the receiver is positioned at the top of a tower, surrounded by a field of mirror surfaces.

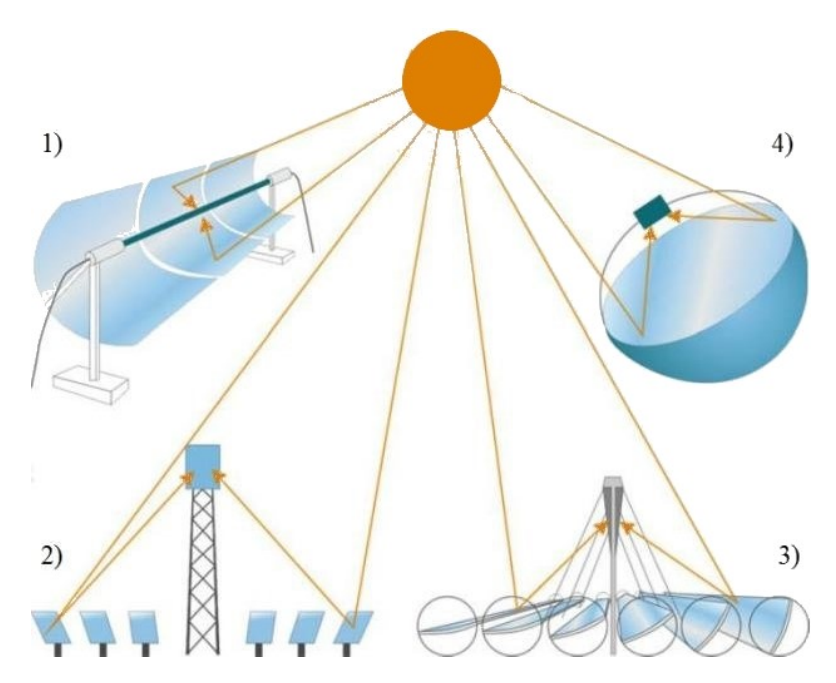


Figure 3: Schematic representation of the four main CSP technologies: 1) Parabolic Trough Collector, 2) Solar Tower, 3) Linear Fresnel Reflector, and 4) Parabolic Dish System [5].

Each mirror is mounted on a structure that tracks the sun in two axes, reflecting solar rays onto the target at the tower.

Parabolic Dish Systems are smaller installations featuring a structure that supports a parabolic-shaped mirror with a receiver above it. The mirror captures solar radiation and reflects it onto the target located at the focal point [4].

2.1.2 Line receiver CSP

In line receiver setups, the mirrors focus sunlight onto a line where a tube is placed. This type is used in both Linear Fresnel and PTC systems.

Linear Fresnel collectors consist of several flat-plane mirrors fixed next to each other. They rotate around their longitudinal axis tracking the sun. The receiver tube is positioned above them [4].

Parabolic Trough Collector

A PTC is composed of a mounting structure, a parabolic-shaped mirror and a receiver tube. Solar rays are concentrated by the mirror on the tube through which the HTF is pumped. The temperature usually reaches up to 400 °C [2]. Several collectors are connected in series before the HTF enters the field pipes leading to the turbine. The collector is tracking the movement of the sun over the day by rotation. Parabolic trough power plants are the most common technology in commercial use [1]. An example is shown in Figure 1.

2.1.3 Tracking

The mirrors need to follow the sun over the course of the day due to the rotation of the earth. Tracking systems ensure the correct placement of the mirrors such that the focus is coinciding with the receiver. Motors adjust the supporting structures of the mirrors based on the location, time, and date.

The tracking type of CSP systems vary: PTCs and Fresnel systems use single-axis tracking, Solar Towers require dual-axis tracking, while Solar Dish Systems do not need tracking. PTCs are unique in that both the mirror and the receiver tube move together. This results from the design, where the receiver tube is mounted on the same structure as the rotating mirror. As a result, the tube remains precisely aligned with the focal line [4].

2.1.4 Heat Transfer Fluid

HTF is used to transport the energy from the receiver to the turbine. Several prerequisites and preferences must be fulfilled: the HTF has to withstand the temperature reached by the solar concentration, have a high heat capacity, remain in the liquid phase over the entire operating temperature range, be non-toxic and non-flammable, commonly available and cheap [6].

2 Fundamentals and State of the Art

Different categories of HTFs are currently used: water, molten salts, synthetic oils, and silicon oils. Water is cheap and environment-safe, but has the disadvantage of evaporation at 100 °C under atmospheric pressure. High pressure in the CSP system is needed to keep it liquid and avoid evaporation in the pipes. In plants using water as HTF, partial evaporation is accepted, leading to complex control systems where the liquid and gas phase coexist [7].

Molten salts allow reaching high temperatures, up to around 600 °C depending on the specific product. However, they solidify below approximately 140 °C, which requires continuous heating and circulation during nighttime or periods without sunlight to prevent solidification inside the pipes. Additionally, material corrosion requires resistant piping and components. Molten salts are commonly used for thermal energy storage, when employed as the HTF, a separate heat exchanger can be avoided [6].

Synthetic oils offer a good heat capacity and stay in liquid phase at the usual operation temperatures, but are flammable and can be toxic. They are currently the most commonly employed HTFs in CSP plants [8]. Therminol® VP-1, a widely used synthetic oil in CSP applications, is an eutectic mixture of biphenyl and diphenyl oxide. Its properties are summarized in Table 1, compared with other available HTFs.

Silicon oils are currently replacing synthetic oils in some plants, as they have a wider operating temperature range and are non-toxic.

Table 1: Characteristics of HTFs at ambient temperature in CSP applications [6][9]

Property	Unit	Therminol® VP-1	Duratherm® S	HITEC®
Type		Synthetic oil	Silicon oil	Molten salt
Freezing Point	$[^{\circ}\mathrm{C}]$	12	-50	142
Max. Temp.	$[^{\circ}\mathrm{C}]$	400	315	535
c_p	$[\mathrm{kJ/kg\cdot K}]$	1.57	1.72	1.85

2.1.5 Rotation and Expansion Performing Assemblies

The connectors between a PTC and the fixed pipes in the solar field are called REPAs. They have to enable the tracking movement of the receiver tube transporting the HTF in the PTCs. Additionally, the temperature changes of the HTF between day and night cause the materials to expand and contract. This translational movement is also absorbed by the REPAs.

REPAs are crucial components in PTC systems, where commercial plants in operation report the greatest maintenance effort. They are under high mechanical stress due to the movements, heat, and pressure inside the pipes. There are two different setups currently in use: Rotary Flex Hose Assembly (RFHA) and Ball Joint Assembly (BJA). This work focuses on BJAs, shown in Figure 4. They consist of three ball joints connected by two tubes, with the ends of the BJA attached to the receiver tube and the field pipe. Each ball joint has one side fixed to a tube, while the other side connects to a tube that can rotate, allowing angular and rotational movement. Inside the ball joints, graphite is used as sealing material.

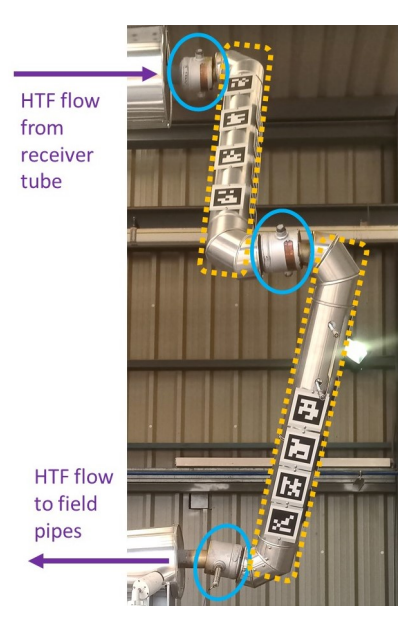


Figure 4: Ball joint assembly for PTCs. Three ball joints (blue circled) are connected by two tubes (yellow dotted, here with insulation).

2.2 REPA test rig

The PSA, located in the Tabernas desert in Southern Spain, is a research, development, and test center for CSP technologies. It is owned and operated by the Spanish CIEMAT, which collaborates with the DLR at PSA. Different experimental setups exist, one of them is a test rig for REPAs. A graphical representation of the test rig is shown in Figure 5 with two flex hose REPAs. For this experiment phase, these have been replaced with BJAs, shown in Figure 4. The test rig is divided in three sections: the main assembly consists of two REPAs, connecting tubes and a kinematic unit for movement. The HTF cycle controls the temperature and pressure of the HTF. A Supervisory Control and Data Acquisition (SCADA) system controls the test rig and collects data during experiments.

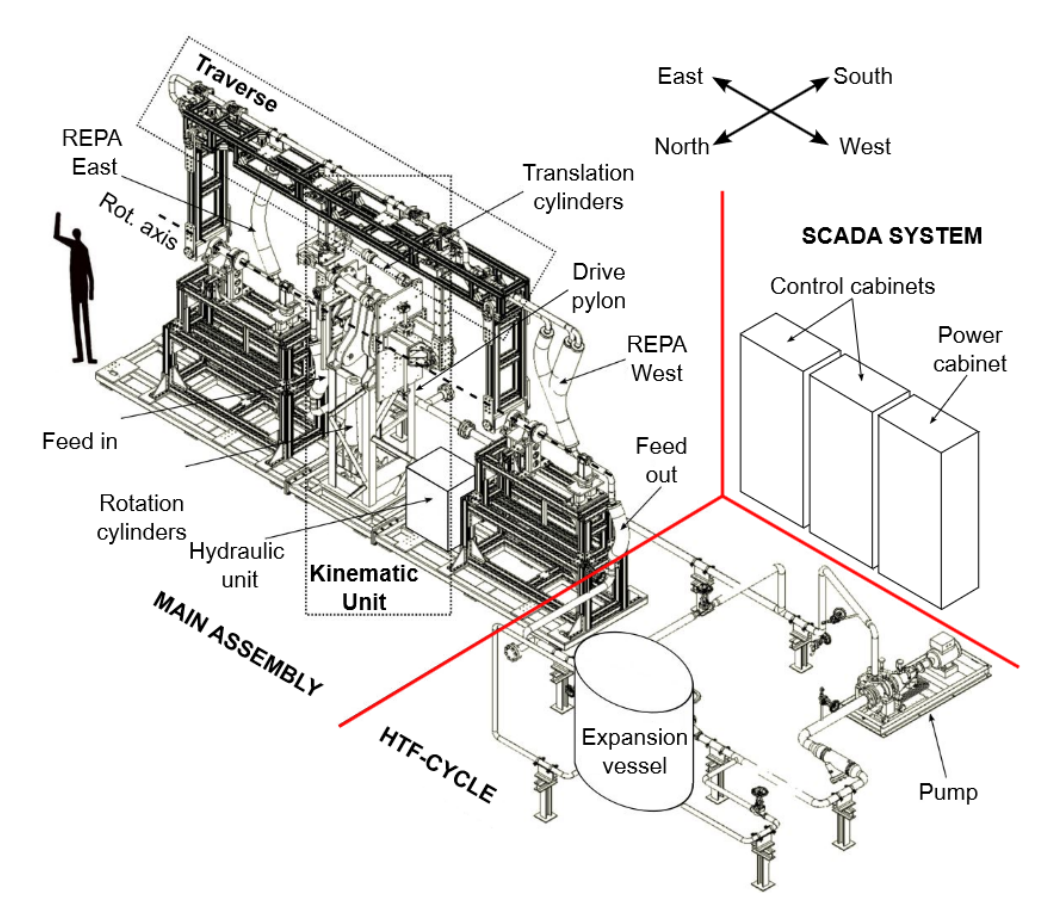


Figure 5: Sketch of the REPA test rig with two flex hose REPAs. For this experiment, they were replaced by ball joint assemblies [10].

The test rig allows accelerated lifetime testing of RFHAs or BJAs. VP-1 is used as the HTF and is heated up to 393°C at a pressure up to 35 bar. It is pumped through a closed loop consisting of two REPAs and connecting pipes, some of which are mounted on a movable traverse. Rotation simulates the daily movement of the mirror and receiver tube as they track the sun. The maximum rotation of the facility is from -23° to 186° . However, the BJA requires to limit the test rig from 0° to 180° . Thermal expansion and contraction of the tubes due to heat-up and cool-down between day and night is represented by a translational movement. The translation angle can be set from -5° to 12° . The setup and movement axes of the test rig with BJAs installed are shown in Figure 2.

The SCADA system controls and monitors the test rig, especially the HTF cycle and the kinematic unit. A graphical user interface is available in LabVIEW [11]. Approximately 10,000 cycles, which correspond to about 19 days of continuous operation in the test rig, represent the estimated 30-year lifetime of a REPA in a CSP plant.

2.3 Cameras for visual observation

Cameras project three-dimensional (3D) scenes onto a two-dimensional (2D) plane. Lens distortion can cause straight lines in the real world to appear curved in the images. Camera calibration is the process of determining parameters that enable correction of this distortion. Pose estimation is the computation of the position and orientation of objects from 3D-2D correspondences. To obtain the necessary 2D coordinates, detection algorithms can identify characteristic objects or markers in the images, with ArUco markers [12] being a popular example for detection. The following section describes the fundamentals of visual observation and the associated pose estimation techniques based on ArUco markers.

The pinhole camera model, shown in Figure 6, explains the projection of a 3D scene on a 2D plane. The camera is positioned at F_c . Points in the real-world, for example the

blue point P with world coordinates X_w, Y_w, Z_w , are projected on the gray uv plane. Its distance from the camera along the optical axis z equals to the focal length f of the camera. The principal point c_x, c_y marks the center of the uv plane. The Brown-Conrady model extends the pinhole model by adding lens distortion factors [13].

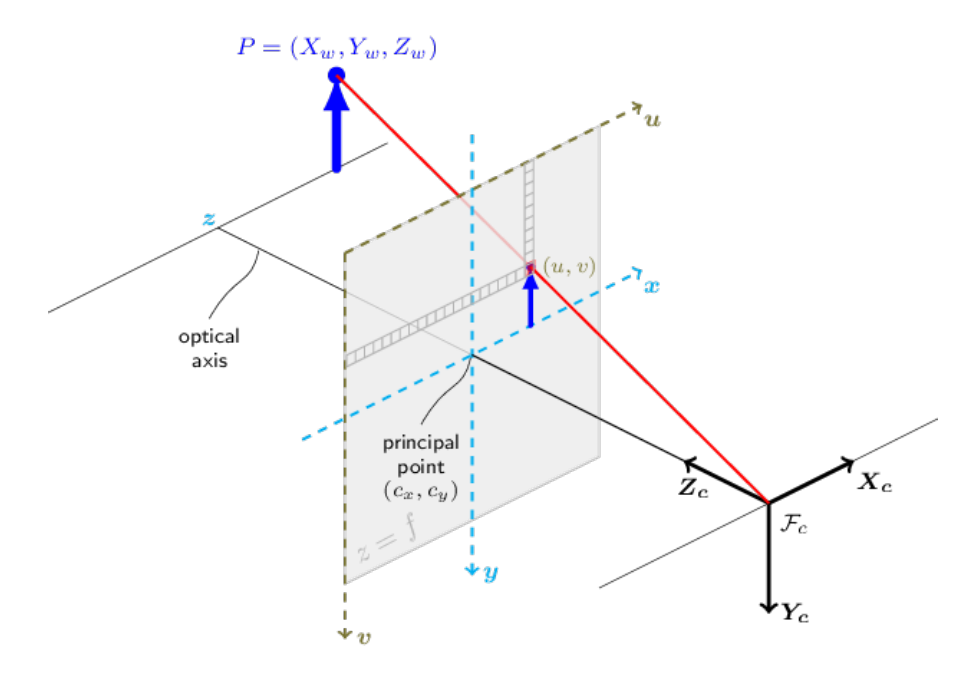


Figure 6: Pinhole camera model projecting a 3D scene onto a 2D plane [14].

2.3.1 Camera calibration

Calibration is the process of identifying parameters of the camera model. They are comprised of the focal lengths (f_x, f_y) , the principal point (c_x, c_y) , and the distortion coefficients $(k_1, k_2, k_3, p_1, p_2)$. These parameters are necessary to enable the correction of lens distortion [15].

A common approach to camera calibration involves the processing of several images of a chessboard from different perspectives. The corners between the black and white squares are detected. The calibration algorithm estimates the camera parameters through geometrical equations [16]. The calibration factors don't depend on the scene but can be applied to all images taken with the specific camera once determined [14].

2.3.2 Pose estimation

Pose estimation is the process of determining the position and orientation (pose) of an object or camera in a known 3D coordinate system, based on a 2D image. The Perspectiven-Point (PnP) problem estimates the camera pose given a set of 3D object points and their corresponding 2D image projections, using the camera calibration parameters.

The estimation computes the rotation and translation vector such that the 3D points, when projected using the camera model, match the 2D points. This is achieved by minimizing the reprojection error, which is the distance between the observed 2D image points and the projected 3D points. The output vectors are given with respect to the Camera Coordinate System (CCS), illustrated with the vectors X_c, Y_c, Z_c in Figure 6.

OpenCV is an open-source computer vision library for Python. Its solvePnP function provides several algorithms for solving the pose estimation problem. The iterative solver SOLVEPNP_ITERATIVE employs the Levenberg-Marquardt algorithm to refine pose estimates by minimizing the reprojection error in a non-linear least-squares framework [17].

2.3.3 ArUco marker detection

To obtain image coordinates, needed for pose estimation, characteristic objects or special markers can be used. ArUco markers are well-suited for this purpose. They consist of a pattern of black and white squares arranged in a square grid, surrounded by a black border. Each marker has a unique ID. Two examples are shown in Figure 7. Multiple dictionaries of ArUco markers exist, varying in grid size and the number of available IDs. Detection software processes images and locates the markers, providing the pixel coordinates of their corners.

ArUco markers also support error correction during detection. This means that even if some grid cells are incorrectly detected, the correct ID can still be determined. The



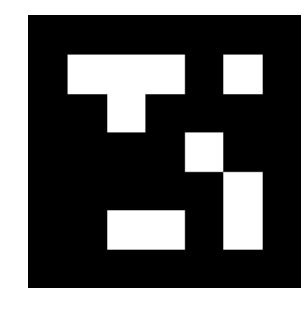


Figure 7: Exemplary ArUco markers with ID 0 (left) and ID 5 (right) [18].

dictionary's Hamming distance defines the minimum difference between any two marker codes, which in turn determines how many detection errors can be identified and corrected [12].

The detection of ArUco markers in an image is done automatically in several steps. The image is first converted to gray-scale. The contours are extracted and filtered for approximate squares. Perspective projection is removed of the internal area of the squares. The grid is applied and each cell is assigned a binary value (zero or one) based on its color, black or white. In a further step, the binary code is looked up in the dictionary. As the marker might be rotated in the image, it is tested in four rotations until a match is found. If no match is found, error correction is applied [12].

Although the detected corners are limited to integer pixel coordinates, subpixel refinement can be performed to further increase the accuracy of marker detection. This process estimates the position of the corner by applying a search window around the detected position, evaluating the transition from black to white along the two marker side axes. The result is a corner position with floating-point pixel coordinates. This refinement is used when high precision of the position is needed, for example in pose estimation [18].

OpenCV has great compatibility with ArUco markers. It offers functions for generating markers of a chosen dictionary and detecting the markers in images including subpixel refinement [18].

2.4 Laser distance measurement

Laser sensors can measure the distance to objects based on different optical methods. In the time-of-flight principle, a laser diode emits a pulsed light beam that is reflected from the object. Measuring the time between sending and receiving the signal, the distance can be calculated taking into account the speed of light in air [19].

2.5 HTF leakage measurement

In CSP, the HTF inside the tubes is usually liquid at high temperature and pressure. When a leak occurs and the HTF exits the tubing, it evaporates due to the lower ambient air pressure. To find and measure HTF leakages, gas concentration sensors for evaporated HTF can be used. They can be specific for a certain gas or measure a set of different chemically similar gases. The gas concentration value in combination with the transport gas flow allows to determine the leakage mass flow.

2.5.1 HTF gas detection

Sensors for detecting gaseous VP-1, the heat transfer fluid (HTF) used in the REPA test rig, were investigated in a previous study [20]. No specific sensor could be found on the market, so sensors for volatile organic compounds were taken into account. They have a chemically similar structure to the synthetic oil used as HTF. Several sensors were pre-qualified and two of these tested for their suitability to detect gaseous VP-1. They were tested with artificially produced VP-1 and air mixtures at different concentrations in a laboratory to verify the reaction on the gas and the relation of the measured value to the prepared concentration value. It had to be expected that the sensors need calibration when detecting the HTF gas. The United Sens-It C₆H₆ was found most useful for the application with VP-1, and then chosen for the further development of the HTF leakage measurement setup [20].

2.5.2 Gas concentration sensor Sens-It

The United Sens-It C_6H_6 sensor measures benzene (C_6H_6) concentration in outdoor air. It is based on a metal oxide semiconductor. Oxygen from the air is adsorbed on the sensor surface, which leads to charge transfer from the semiconductor material to the oxygen molecules. When the benzene gas interacts with the adsorbed oxygen via redox reactions, electrons are released back into the conduction band of the semiconductor. This change in charge carrier concentration leads to variations in the sensor current, which can be correlated to the concentration of the gas. The selectivity of the gas to detect is reached through special doping of the semiconductor [21].

The measuring range of the sensor for benzene is 0.1 ppb to 30 ppb with a precision of 0.2 ppb and a resolution of 0.1 ppb [21]. The measurement values recorded by the Sens-It range from 0 ppb to 36.5 ppb.

The calibration for VP-1 was performed with mixtures of different concentration values. The results are shown in Figure 8. Three test series were done with initial mixtures of VP-1, nitrogen, and oxygen that were diluted twice. The measurement ratio x_r describes the ratio between the prepared mixture and the measured value. Limits in the test setup didn't allow for lower artificially mixed concentrations in the measuring range of the sensor.

2.5.3 HTF leakage measurement system

A prototype for a HTF leakage measurement system was developed by Hardelt, described in [20]. The necessary sensors are attached along a plastic pipe with a diameter of 75 mm and a length of 2 m. A Raspberry Pi microcomputer reads the data and controls a fan at the end of the pipe that generates the air flow.

Along the pipe, a United Sens-It C_6H_6 sensor, as well as air flow speed, temperature, and pressure sensors, are installed. The air flow is regulated by adjusting the fan speed. It is

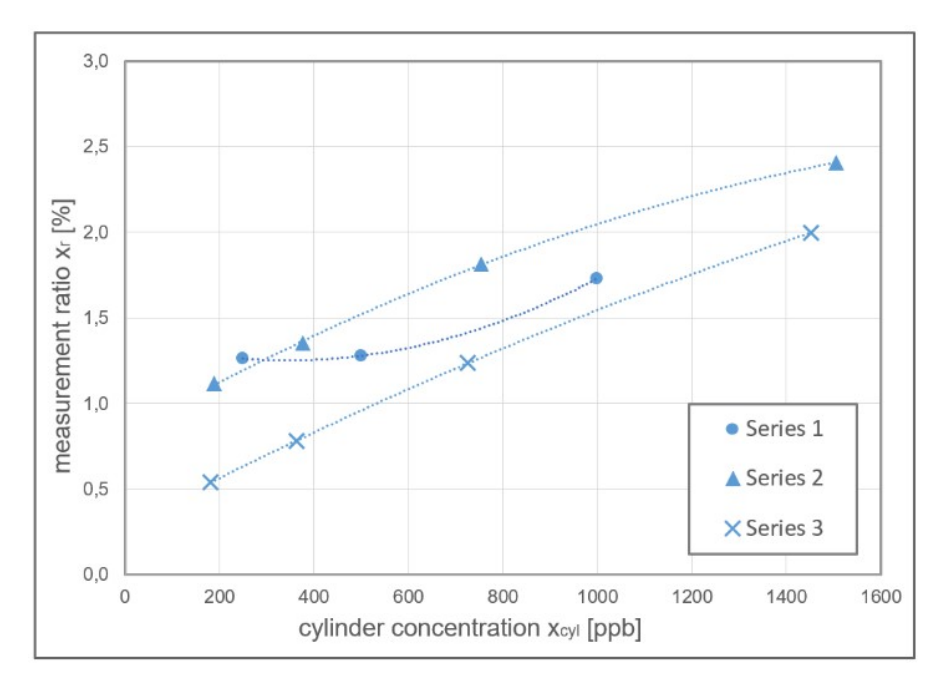


Figure 8: Ratio of cylinder concentration (containing a mixture of VP-1, N_2 , and O_2) and the measured value of the Sens-It sensor [20].

increased or decreased as the gas concentration approaches the upper or lower limits of the measurement range, to dilute or concentrate the air-gas mixture in the pipe [20].

3 Experimental Setup

Two REPAs are currently integrated into the test rig and tested simultaneously. These REPAs are of the BJA type, each consisting of three ball joints connected by two tubes. The test rig, shown in Figure 2, is equipped with various sensors to monitor the behavior during the experiment. This work integrates three cameras, a laser distance sensor, and a HTF leakage sensor. Their setup is described in the following sections.

3.1 Geometric transformation observation

Visual observation using cameras and a laser sensor that measures the distance to targets allows to analyze geometric transformation of the REPA tubes during the experiment. Integrating different observation methods for the same mechanical parts enables for comparison of measurements and cross-checking. The setup and working principles of the two approaches are explained below.

3.1.1 Cameras

Three cameras are installed to monitor changes in the angles of the connecting tubes. Each camera observes one REPA from a different side. Cameras A and B, which observe the western REPA, have a resolution of 3072×2048 pixels, while camera C, observing the eastern REPA, has a resolution of 2048×1536 pixels. The cameras are connected via LAN to the test rig control computer, which runs a LabView program to capture and

3 Experimental Setup

store the images whenever predefined rotation angles of 70°, 80°, 90°, 100° and 110° are reached, along with the corresponding rotation and translation values of the test rig.

ArUco markers with a side length of 80 mm are firmly attached to the REPAs and to fixed and rotating parts of the structure. Each REPA tube is equipped with four ArUco markers on each side that is facing one of the cameras. While two markers would be sufficient to determine the tube's orientation, two more are added to increase redundancy and mitigate detection failures.

The setup with the position of the cameras and the ArUco markers is shown in Figure 9. For each camera view, four markers are attached to the rotating part of the test rig to define reference positions, forming a coordinate system that rotates with the traverse. Additionally, two markers are fixed at the non-moving part of the structure, which are used to evaluate the precision of the detected marker corner coordinates.

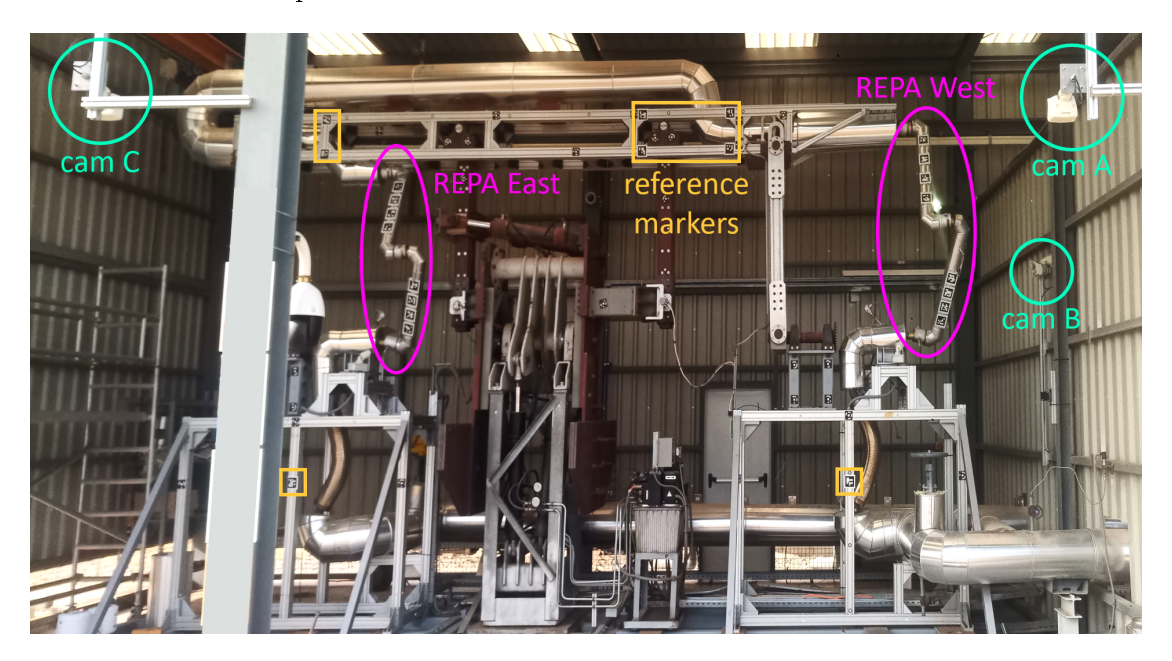


Figure 9: Setup of three cameras (cyan circles) and reference ArUco markers (orange squares) at the test rig. The tubes of the east and west REPA (purple ovals) are equipped with ArUco markers.

3.1.2 Laser distance sensor

A laser distance sensor is installed at the wall next to the test rig. It continuously measures the distance to the nearest obstacle in its line of sight. A target, consisting of a metallic plate covered with paper tape to reduce laser beam scattering, is attached to the lower tube of each REPA and crosses the laser beam at a specific rotation angle of the test rig. The two targets are positioned such that the laser can detect these one after the other with a gap between them while the test rig is rotating. The setup is visualized in Figure 10.

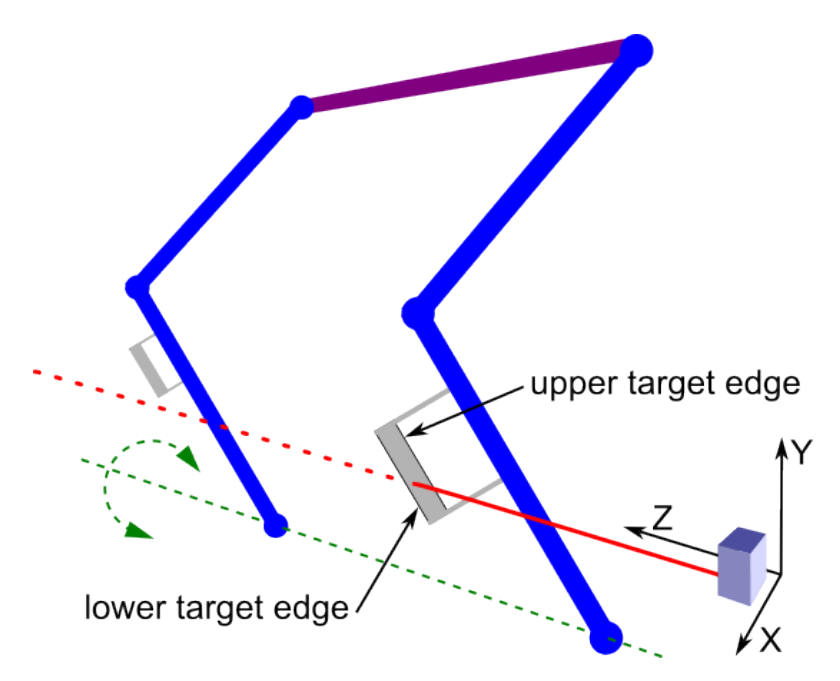


Figure 10: Schematic of the two REPAs (blue) with one target at each lower tube (gray). The test rig is rotating around the green dashed-marked axis. The targets cross the laser beam (red, the dashed part is the imaginary continuation of the beam).

By measuring the distance to each target throughout the experiment, distance changes of the targets along the Z-axis can be detected. Additionally, the rotation angle of the test rig at the moments when a target enters and exits the laser beam, detecting their edges, is stored and used to determine tube position changes in the XY-plane.

3.2 HTF leakage sensor

The HTF leakage sensor, described in detail in Chapter 2, consists of several sensors arranged along a plastic tube. The United Sens-It sensor measures the gas concentration in the air flowing through the pipe. Additionally, the ambient temperature, pressure, and the flow speed inside the pipe are stored. A Raspberry Pi microcomputer logs all data and controls the fan at the end of the pipe that generates the airflow. The leakage sensor is installed near the lowest ball joint of the eastern REPA as shown in Figure 11. Constructing a sealed box around the ball joint to capture all exiting gases and channel them into the pipe was planned but not feasible due to mechanical movement and space constraints. Therefore, the pipe entrance was placed as close as possible to the insulated ball joint.



Figure 11: HTF leakage sensor installed at the test rig with the entrance of the pipe near one ball joint (here shown without its insulation).

4 Methodology

This chapter describes the experiment conducted on the REPA test rig. After installing the HTF leakage sensor, the three cameras, and the laser distance sensor as described in Chapter 3, the HTF was heated, and the cycling process started. The different experimental phases are described in detail, followed by an explanation of the data evaluation methods applied to the various measurements.

4.1 Experiment phases

The experiment follows a specific routine consisting of a heat-up phase before the cycling process. During the first experiment, a nationwide power outage caused an unexpected stop of the cycling and cool-down of the HTF, a second experiment was carried out after restarting the facility.

4.1.1 Heat-up phase

The REPA test rig operates with HTF at approximately 393°C to simulate real-world conditions in the PTC receiver, where heating occurs daily via solar radiation. The heat-up process is carried out in several steps to ensure consistent temperature distribution throughout the HTF and to allow the tubes and ball joints containing the HTF to reach thermal equilibrium. Initially, the HTF was electrically heated to 250°C and maintained at this temperature for one day. Subsequently, it was heated to 350°C and stabilized

for another day before being further heated to the target temperature of 393 °C, which was then held constant. During the heat-up phase, pressure increased up to 35 bar due to the temperature rise and the addition of nitrogen to the expansion vessel. Figure 12 shows the temperature and pressure of the HTF throughout the heat-up phase.

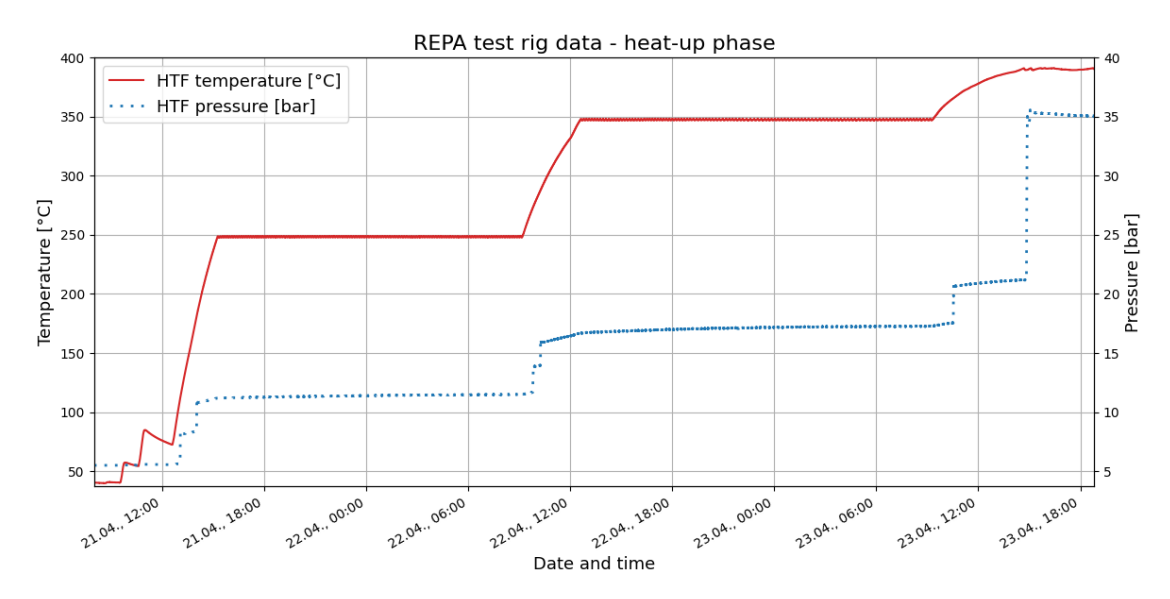


Figure 12: Temperature and pressure of the HTF during the heat-up phase. Heating is carried out in several steps to allow temperature stabilization.

4.1.2 Cycling phase

The cycling phase of the test rig begins once the HTF temperature has stabilized. The traverse rotates from 0° to 180° position and back with an average speed of approximately $1.54^{\circ}\,\mathrm{s^{-1}}$. This movement simulates the tracking of the sun's position over a day by a PTC. Additionally, a translational movement simulates the expansion and contraction of the receiver tube due to material heating and cooling. The translation angle cycles between -5° and 8.5° . Both movements are shown in Figure 13. Note that the plotted values do not exactly reach their maximum and minimum because positions are recorded only every five seconds. During this phase of the experiment, 2,700 cycles were completed.

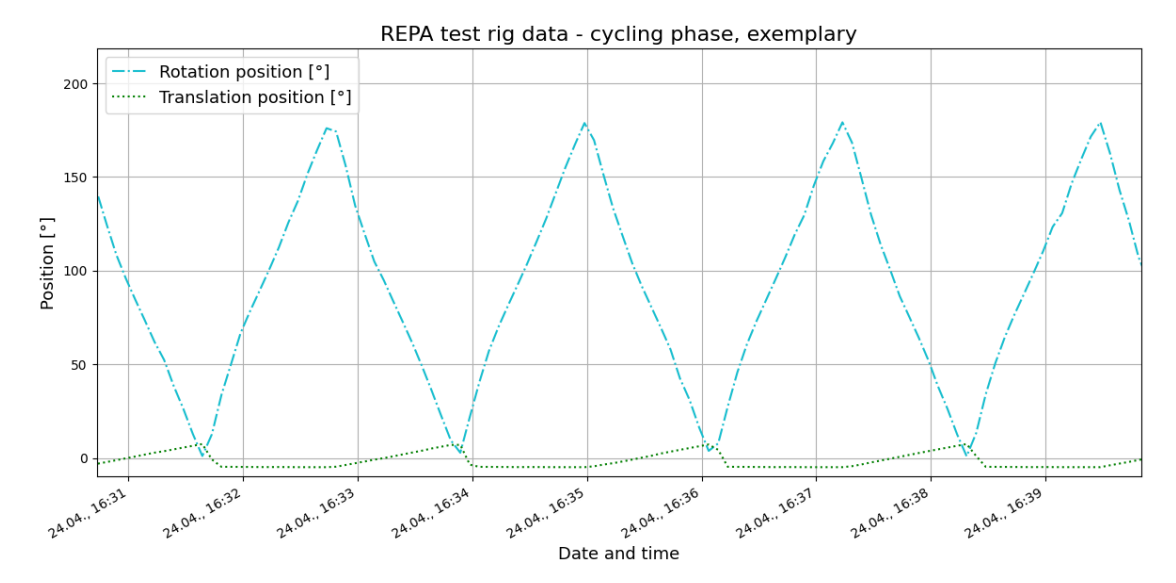


Figure 13: Exemplary snippet of the cycling phase of the REPA test rig. The rotational and translational movements follow a fixed pattern throughout the cycling phase, simulating real-world movements in a PTC.

4.1.3 Maintenance phase

Due to a nationwide power outage in Spain on April 28, 2025, the facility experienced an unexpected shutdown. The electrical heaters were unable to maintain the HTF temperature, which cooled down to ambient levels. The cycling with rotational and translational movements stopped.

Upon reheating the test rig after the grid was restored, strong visible outgassing was observed at all ball joints, indicating HTF leakage. The insulation around the ball joints was removed to better monitor this effect. Condensed leaked HTF was visible near the ball joints and on the inside of the insulation. The completed 2,700 cycles correspond to a lifetime of approximately seven years.

To mitigate the outgassing, maintenance was performed on the ball joints by refilling graphite, the recommended sealing material by the manufacturer. The ball joints themselves were not replaced.

4.1.4 Second experiment phase

After maintenance was carried out, the HTF was heated again in steps to $370\,^{\circ}$ C. The pressure was set to $20\,\mathrm{bar}$. During the following cycling phase, translational movement from -4° to 12° was applied only for the first twenty cycles. After that, the translation was kept constant at an angle of -3.4° , representing the position of the REPAs in a PTC during daytime with hot HTF. In total, $40\,\mathrm{cycles}$ were performed. Afterwards, the temperature of the HTF was kept constant at $250\,^{\circ}$ C. Ongoing outgassing was observed in the following days, therefore, the facility was cooled down to add more graphite to the affected ball joints. No further evaluable data was generated from the test rig for this work.

4.2 Data evaluation

During the above described experimental phases, images and sensor readings were captured and afterwards analyzed. The methods for data evaluation depend on the sensor type and are explained below.

4.2.1 Cameras

Throughout the experiment, changes in the angle of the connecting pipes of the REPAs can be observed by detecting the ArUco markers in the images and referencing their position relative to the rotating part of the structure. The images taken at predefined angles in every fifth cycle of the test rig are processed in several steps by Python scripts.

First, ArUco markers are detected in each image using the corresponding function of the OpenCV library. An exemplary image of camera A with the detected markers and their IDs is shown in Figure 14. The output of this process consists of the pixel coordinates of the four corners of each marker, along with its ID.



Figure 14: Exemplary image of camera A with the detected markers and their unique IDs. Here, not all markers were detected along the lower tube.

Sub-pixel refinement is applied to further improve the estimated position of the corners. The next step estimates the 3D positions of all markers using OpenCV's PnP solver. It processes the detected corner coordinates and the known physical dimensions of the markers to compute the position of each center in the real world, yielding the X_c, Y_c, Z_c coordinates, expressed with respect to the CCS.

To avoid dependence on the test rig's rotation angle, a coordinate transformation is performed to relate the markers' positions to a Reference Coordinate System (RCS). The estimation of the RCS with respect to the CCS is based on four reference markers attached to the rotating part of the test rig for each camera perspective. Figure 15 shows the view of camera B at a test rig rotation angle of 90.6° with the detected markers. The origin of the RCS lies in marker 32, the positions of the other markers are then expressed relative to that coordinate system.

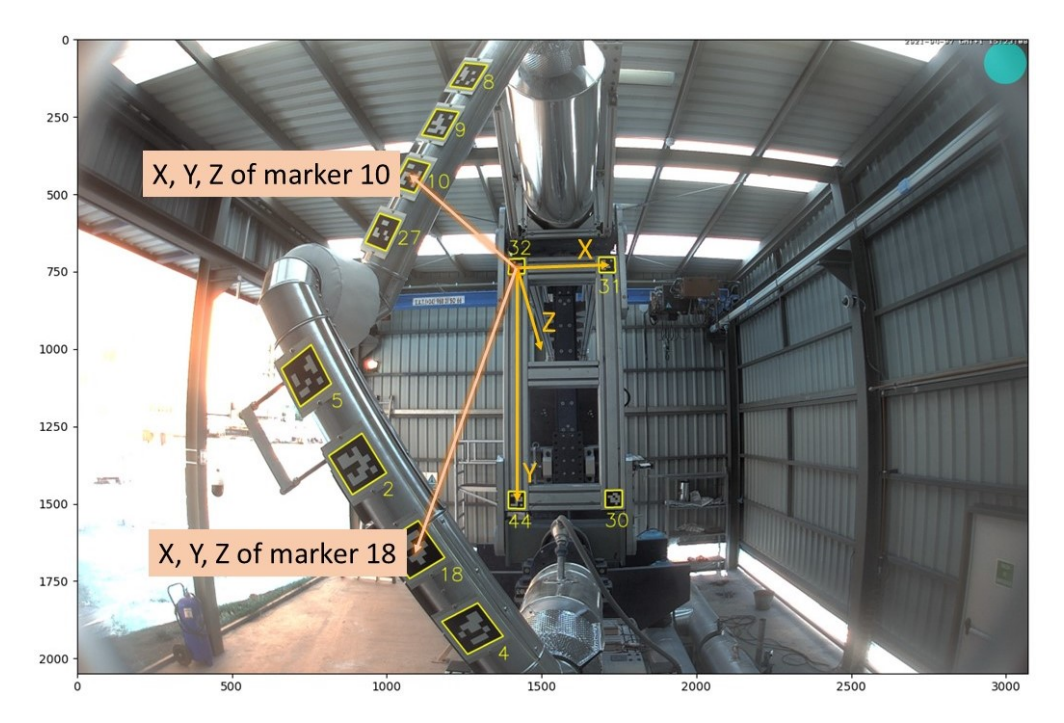


Figure 15: Exemplary view of camera B with the detected markers and their unique IDs. Four markers on the rotating structure form the RCS (yellow). The positions of the markers on the tubes are given with respect to its origin (orange).

The 3D positions of the markers attached to the REPA tubes with respect to the RCS allow representation of the two tubes by fitting a line through them. The fitting algorithm minimizes the distance between the estimated marker positions and the line. For the fit, all detected markers are used. The distance of each marker to the line is calculated, and a second line fit is performed using the three markers closest to the initial line, increasing robustness against outliers due to inaccurate detection.

The vectors of these lines are used to calculate the angles between the tubes and of each tube separately projected onto the XY and YZ planes of the RCS. These angles, clustered by test rig rotation angle, are evaluated over the experiment duration.

4.2.2 Laser distance sensor

The laser distance sensor measurements are compared over the experiment duration. For each cycle, the distance values to the two targets, as well as the test rig rotation angle when their edges cross the laser beam, are used for analysis. Unrealistic values suggest difficulties in detecting the target edges and are therefore filtered out.

4.2.3 HTF leakage sensor

The measurements of the several integrated sensors are compared during the heat-up, cool-down, and cycling phase. In addition to visualization over time, dependence of gas concentration on the number of completed cycles, the HTF pressure, the ambient temperature, the HTF temperature, and its evolution is analyzed. The data is also clustered by the experiment phases for correlations at working conditions (relating to daytime in a CSP plant), transient phases and cold HTF temperature (relating to nighttime, cloudy days, or shutdown of a CSP plant).

5 Results

This chapter presents the results derived from the data collected during the experiment using the setup described in Chapter 3 and analyzed according to the methodology detailed in Chapter 4. The results are shown for the visual geometric transformation observation and the HTF leakage sensor.

5.1 Geometric transformation observation

The cameras and the laser distance sensor observe the geometric structure of the two REPAs installed at the test rig. The data of both measurement devices is processed to determine whether there is an angle change of the tubes connecting the ball joints.

5.1.1 Image analysis

The camera images are supposed to be taken at predefined test rig rotation angles of 70°, 80°, 90°, 100° and 110° in every fifth cycle. In reality, the moment of image capture does not coincide exactly with these rotation values due to processing and storing time.

The ArUco markers attached to the test rig are well detected in images taken at daytime. Due to bad lighting conditions, only some markers can be detected in the nighttime images. Further analysis is carried out on images in which the required markers are detected.

The three cameras A, B, and C, observe the test rig from different perspectives. A fixed marker, identified with ID 41 in Figure 14 and observed by camera A, is used to assess the precision of corner coordinates detection. The influence of detection noise on the estimated 3D position of the marker is evaluated.

The estimated coordinates of the fixed marker vary between images per corner in both the X and Y directions by mostly zero to two pixels, with a maximum deviation of up to four pixels. Although the marker is physically square, it appears approximately 29×27 pixels in the image due to differences in the camera's resolution along the width and height and the observation from above.

Figure 16 shows the resulting 3D position displacement plotted against the cumulative corner pixel shifts, relative to the initially detected coordinates and estimated position. Additionally, the figure includes the frequency distribution of the cumulative pixel shifts. The observed noise causes significant variations in the estimated 3D marker positions. Typically, cumulative pixel shifts range from two to eight pixels and correspond to physical displacement of 0 cm to 20 cm. A greater cumulative pixel shift does not necessarily correspond to a larger displacement in real-world coordinates.

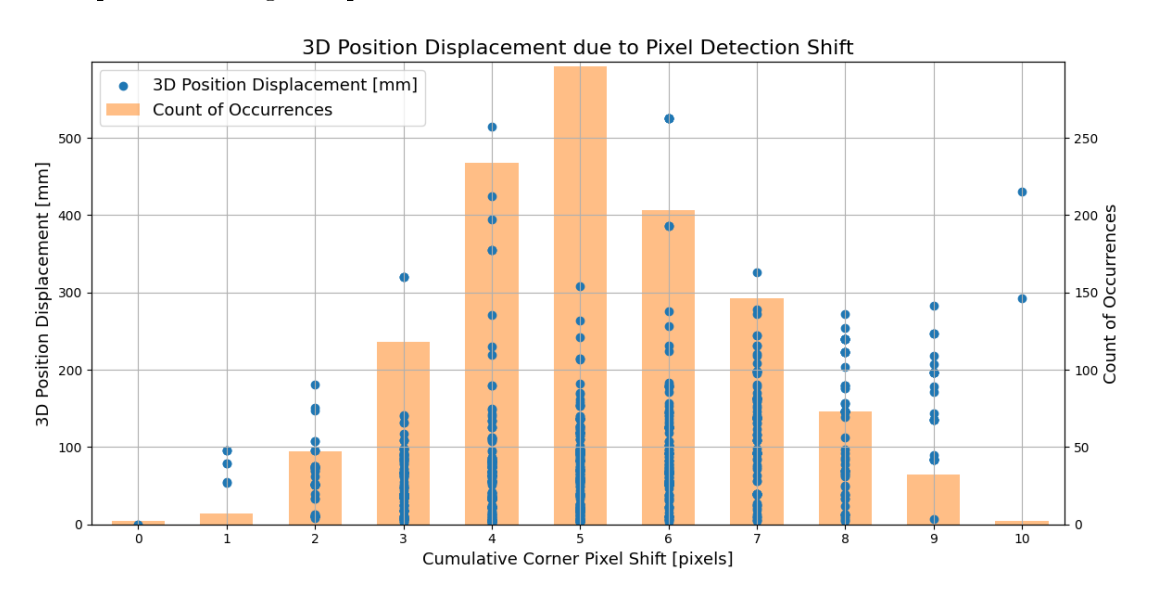


Figure 16: Influence of corner pixel shifts on 3D position for a fixed marker. Bars show the occurrence count of each cumulative pixel shift.

A further analysis evaluates the influence of detection noise on all markers captured by the three cameras. To simulate noise, the corner coordinates of all markers are artificially perturbed in 100 different ways, using combinations of pixel shifts ranging from zero to three pixels per corner and direction. Each perturbation results in a cumulative pixel shift ranging from one to ten pixels across the entire marker. For each perturbed case, the marker's 3D position is estimated, and its distance from the base (unperturbed) position is calculated.

The influence is shown in Figure 17, where the average distance per shifted pixel is plotted for each marker, grouped by camera. The distance depends on the camera and specific marker. Camera B is installed closest to the test rig and the markers, therefore, the markers appear larger in its images. Camera C has a lower resolution than the two others, so the relative pixel shift is higher compared to the pixel size of a marker.

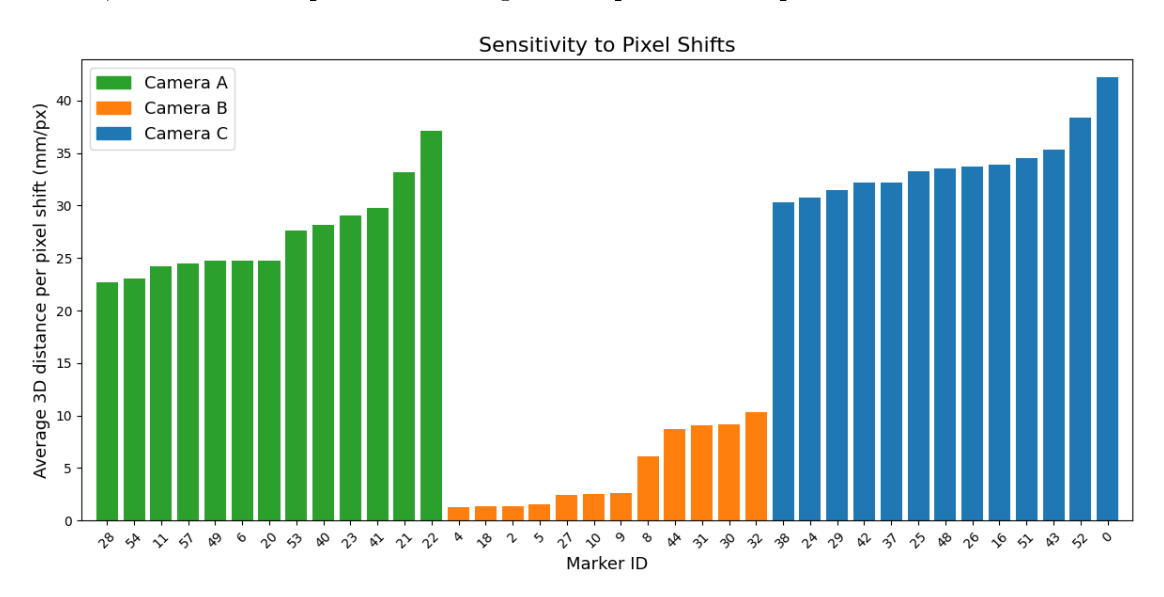


Figure 17: Sensitivity of 3D displacement to pixel shift for all markers.

Concluding, the sensitivity of the 3D position to pixel shift due to detection inaccuracy is lower for larger (appearing) markers. The markers observed by camera B with their IDs are shown in Figure 15. The markers closest to the camera, attached to the lower REPA tube, show the least average 3D distance per pixel shift.

The detection of the marker corners cannot be improved in the scope of this work. Therefore, the further analysis is done with the images of camera B only, where the influence of pixel shift is smallest. It observes the western REPA. The detected marker positions are refined with subpixel accuracy and the 3D position of the markers is estimated based on the refined pixel corner data.

The 3D positions of the markers detected by camera B are transformed into the RCS, which moves with the rotating part of the test rig. Through this, the influence of deviation in the rotation angle of the images is avoided. The estimated positions of the markers, camera, CCS and RCS for an exemplary moment are shown in Figure 18. Markers with IDs 8, 9, 10, and 27 are attached to the upper BJA tube, while markers with IDs 5, 2, 18, and 4 are attached to the lower tube.

Camera, Coordinate Systems and Marker Visualization

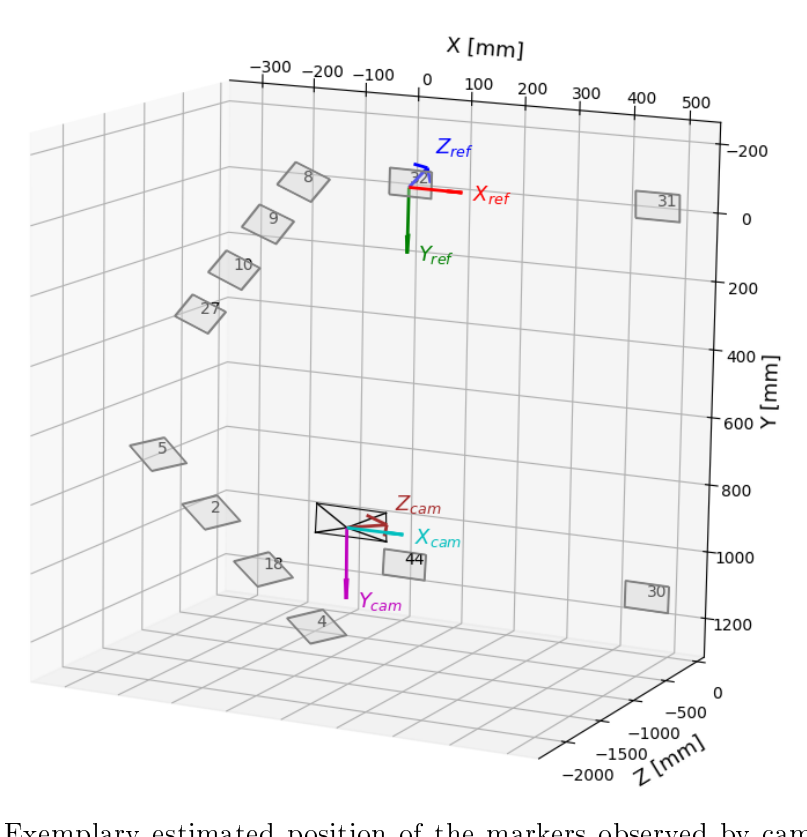


Figure 18: Exemplary estimated position of the markers observed by camera B with the CCS and the RCS.

Line fits and tube angles

Several angles are derived from the estimated positions of the markers attached to the two tubes of the western REPA. The 3D angle represents the angle between the two tubes, indicating the degree of rotation required to make one tube parallel to the other. Additionally, the tubes are projected onto the XY and YZ planes to observe angle variations from two different perspectives. These projections give angles in an assumed two-dimensional setup. The coordinate system is illustrated in Figures 15 and 18.

Each tube is also analyzed individually. Its angle relative to the horizontal (ground) plane is calculated based on its projections onto the XY and YZ planes. Using these angles, both the individual tube orientations and the angles between the tubes are examined from different perspectives. Cycles performed during nighttime have lower-quality vision and marker detection with increased noise, therefore, these cycles are filtered out.

In the mechanical setup, markers attached to each REPA tube lie along a straight line. However, inaccuracies in marker corner detection and subsequent pose estimation introduce errors. To assess the impact of these inaccuracies on the calculated tube angles, two different vectors are derived for each REPA tube and compared.

The first vector is obtained by fitting a line through all estimated marker positions of the respective tube. Since not all markers coincide with this line fit, the distances of all estimated marker positions to the fitted line are calculated. For comparison and refinement, a new line fit is performed using only the three markers closest to the initial line. This approach ignores the most outlying marker, assuming it results from detection inaccuracies.

Figure 19 illustrates the two line fits for the upper tube at an exemplary moment, where the distance of the furthest marker to the initial fit is 90.26 mm. The refined fit based on the three closest markers shows a different line orientation, demonstrating the effect of excluding the outlier.

5 Results

Marker positions and line fits X [mm] -350 -300 -250 -200 -150 -100 -50 0 50 Initial tube fit Refined tube fit Markers for refined fit -200 -1000 -1100 -1200 -1300 -1300 -1400 -1500

Figure 19: Marker positions and line fits based on all detected markers and on the three markers closest to the initial line for the upper tube.

The average and maximum distance of the markers from the two line fits for all cycles performed at daytime are given in Table 2. The maximum and average distance resulting from the new fit is reduced for both tubes. The average distance is smaller for the lower tube, where the camera is closer to the markers.

Table 2: Maximum and average marker distance to the two line fits. One is based on all markers, the other on the closest three markers to the initial fit.

Tube	Distance to line fit	Fit based on all markers	Fit based on closest 3 markers
Upper	$egin{aligned} ext{Maximum} \ ext{Average} \end{aligned}$	$90.26\mathrm{mm}$ $2.67\mathrm{mm}$	$46.21\mathrm{mm} \\ 1.53\mathrm{mm}$
Lower	Maximum Average	$35.04\mathrm{mm}$ $1.69\mathrm{mm}$	$24.04\mathrm{mm}$ $1.15\mathrm{mm}$

The difference in the resulting tube angles between the two fits is calculated and plotted against the reduction in the distance of the farthest marker to the fitted line in Figure 20. This variation in angles reflects the impact of marker pose estimation inaccuracy.

Overall, the angle differences are small, generally within $\pm 1^{\circ}$ for the upper tube, except for a few extreme cases, and less than 1° for the lower tube. A trend of increasing angle difference with greater marker distance reduction is observed. This supports the approach of excluding the outlier, as markers farther away have a stronger influence on the tube angle.

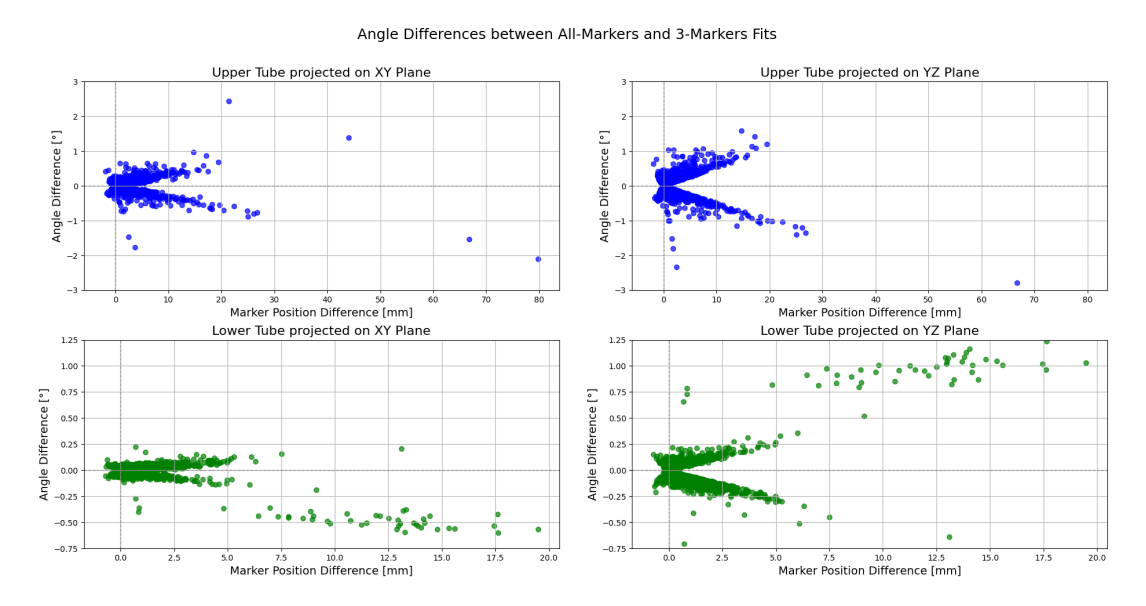


Figure 20: Tube angle difference resulting from excluding the farthest outlying marker position.

To calculate the tube angles with high accuracy, measurements are filtered based on the distance of the estimated marker position from the line fit based on three markers. If any of the markers is farther away from the fit than a threshold value of 3 mm, this data point is removed. This threshold value is chosen based on the average distance of the markers, keeping it as small as possible for high-quality output data, but allowing for small mechanical inaccuracy in the marker installation.

The angles are shown in Figure 21. Gray vertical lines indicate cycles where the data point was filtered. As expected, filtering mostly affects cycles performed during nighttime, which were already excluded. Overall, the different angles vary from cycle to cycle without showing a clear pattern or trend.

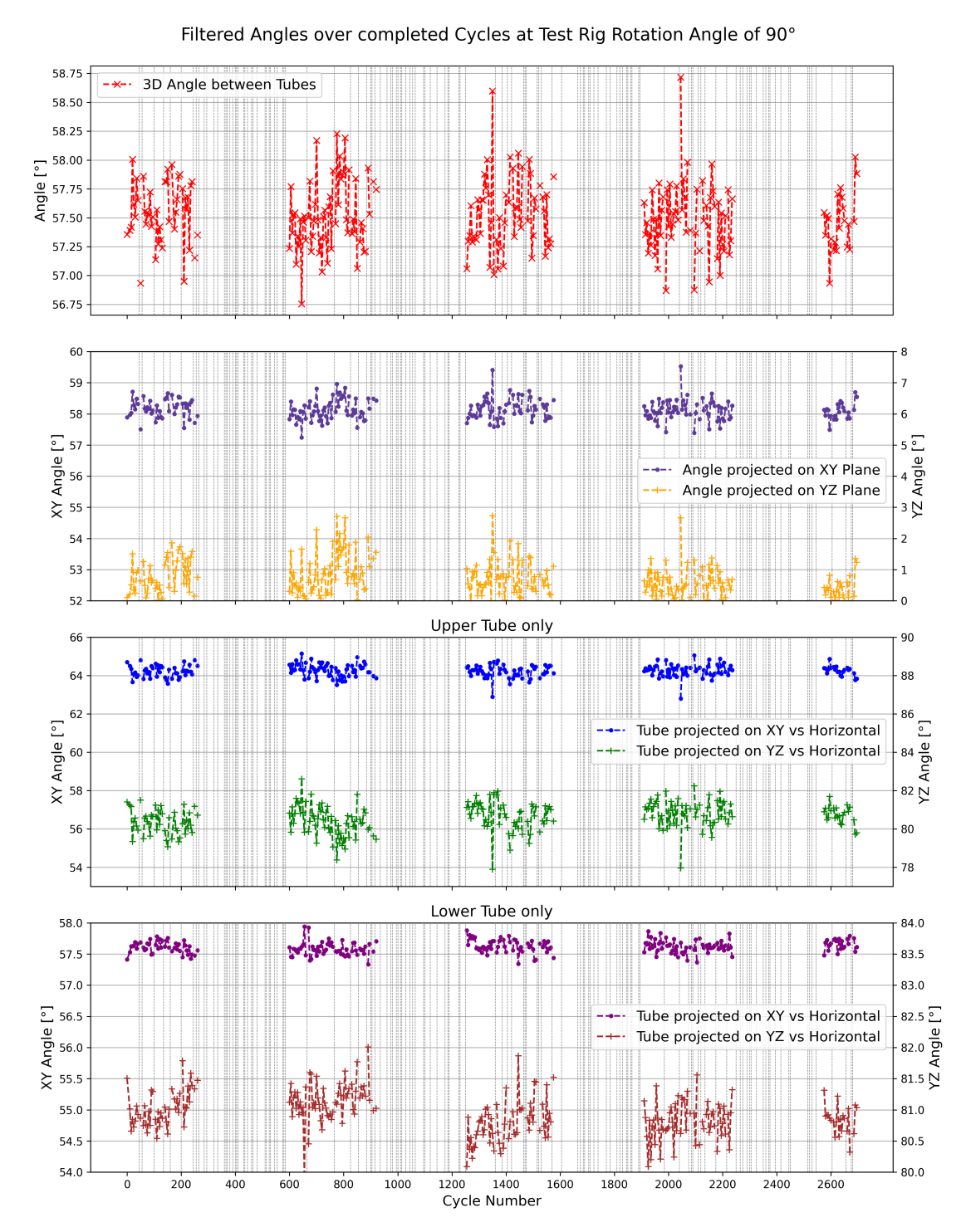


Figure 21: Angles over completed cycles at a test rig rotation angle of 90° descending. Filtered data points are indicated by gray dashed lines.

A linear fit is applied to the estimated angles over completed cycles to quantify potential long-term trends. Table 3 summarizes the mean, minimum, maximum, standard deviation, and slope of the linear fit for each angle. The slopes are very close to zero, indicating that no significant long-term trends are present in any of the angles throughout the experiment. Additionally, the narrow range between minimum and maximum values, along with low standard deviations, prove only minor fluctuations in tube angles over the testing period. The angles projected on the YZ plane show slightly greater variability compared to those on the XY plane.

Table 3: Tube angle statistics: mean, standard deviation (std), minimum, maximum, and linear fit slope over cycles.

Metric	Mean [°]	Std [°]	Min [°]	Max [°]	Slope [m°/cycle]
3D angle	57.52	0.30	56.75	58.72	-0.02
Angle on XY Plane	58.14	0.33	57.24	59.53	-0.02
Angle on YZ Plane	0.73	0.57	0.00	2.73	-0.14
Upper tube XY angle	64.23	0.71	54.51	65.15	0.01
Upper tube YZ angle	80.54	1.49	60.73	82.67	0.20
Lower tube XY angle	57.59	0.22	55.33	57.94	0.03
Lower tube YZ angle	80.98	0.60	79.89	86.46	-0.16

5.1.2 Laser data analysis

The laser sensor measures the distance to the targets attached to the lower tube of each REPA. Additionally, the rotation angle of the test rig is recorded at the moments when the upper and lower edges of the target cross the laser beam. Laser data are not available for the first cycling phase before the power outage, so the results presented focus on the 40 cycles of the second period, during which the ball joint assemblies were already used. The translation angle movement was active during the first 19 cycles and held constant at -3.4° thereafter.

Figure 22 shows the distances from the laser sensor to the upper and lower edges of the target on the eastern REPA. Since the target is positioned perpendicular to the laser

beam, the distances to both edges are expected to be identical. Cycles where these two distance values differ (e.g., cycle five) can be filtered out, as such discrepancies indicate faulty edge detection or other measurement issues.

In the first few cycles following maintenance, the distance values show variation corresponding to the settling process of the ball joints. During this period, translational movement was applied to assist the settling. Once the translation angle was fixed, a stable distance to the target was established.

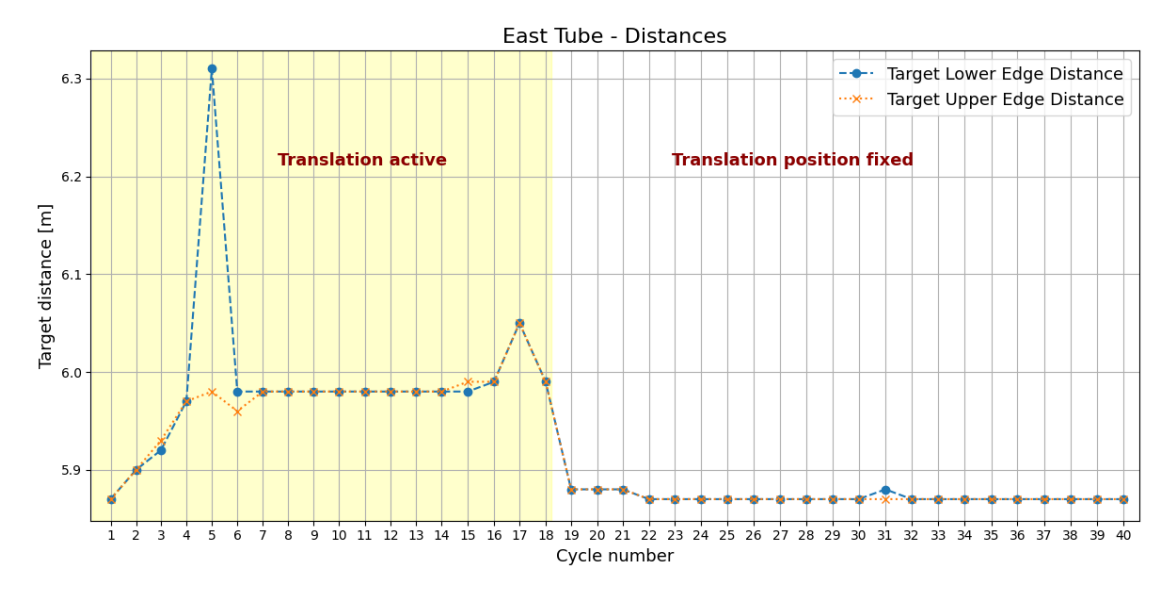


Figure 22: Distance to the eastern REPA target's edges over 40 cycles. The yellow-highlighted cycles indicate when the translation angle of the test rig was moved, after which it was held constant.

The test rig rotation angles at the eastern and western target edges, as well as the distances for the western REPA, are analyzed following the same procedure as above. For each cycle, multiple values were stored, suggesting that the targets were detected more than once at different positions. The recorded distances and rotation angles vary over a range larger than what can be expected from the mechanical setup. In some cases, the upper and lower edges cross each other. Due to these issues in the measurement and data storage process, further analysis of this data is not feasible.

5.2 HTF leakage sensor measurements

The gas concentration in the pipe of the HTF leakage sensor is measured by the Sens-It benzene sensor along other values. The pipe is fed with air near one of the insulated ball joints. HTF leaking from the ball joint evaporates due to the lower ambient pressure, mixes with the surrounding air, and is detected by the Sens-It sensor.

5.2.1 HTF leakage time series

The gas concentration along other values is shown in Figure 23 for all experiment phases. The time frame where the 2,700 cycles were performed is marked. During the cycling phase, the measured concentration values stay low.

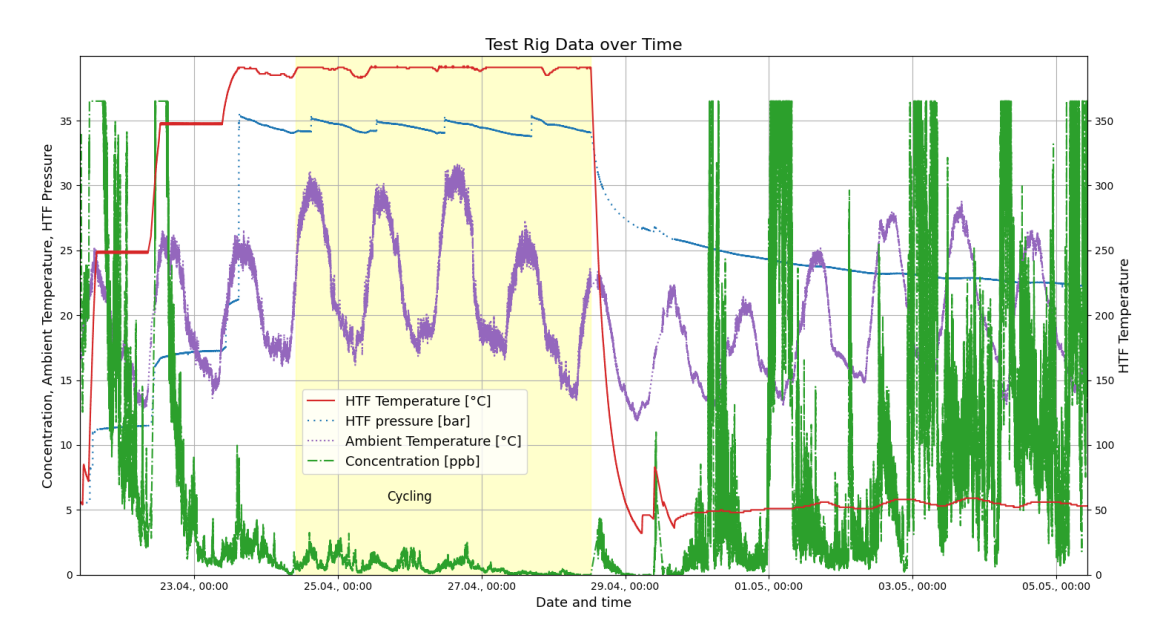


Figure 23: Measurement data over the whole experiment, the cycling phase is marked.

In more detail, the measurements for the separate phases are described in the following. During the heat-up phase, the HTF is heated and pressurized in steps to 393°C and 35 bar. In a CSP plant, heat-up and cool-down occur daily along the rise and set of the sun. In the test rig, this phase is run once before starting the cycling phase. The

measured gas concentration and airflow speed in the pipe during heating are shown in Figure 24. Shortly after the start of heating, the gas concentration is reaching 36.5 ppb, which is the maximum of the sensors measuring range. The setup foresees controlling the fan speed to increase airflow and, through dilution, reduce the concentration. The fan speed is increased up to its maximum, causing the flow speed to reach the upper limit of the corresponding sensor at 4 m/s. However, the concentration remains at its maximum value until approximately three hours after the HTF stabilizes at 250 °C. The same effect can be seen the following day during and after the next heat-up step.

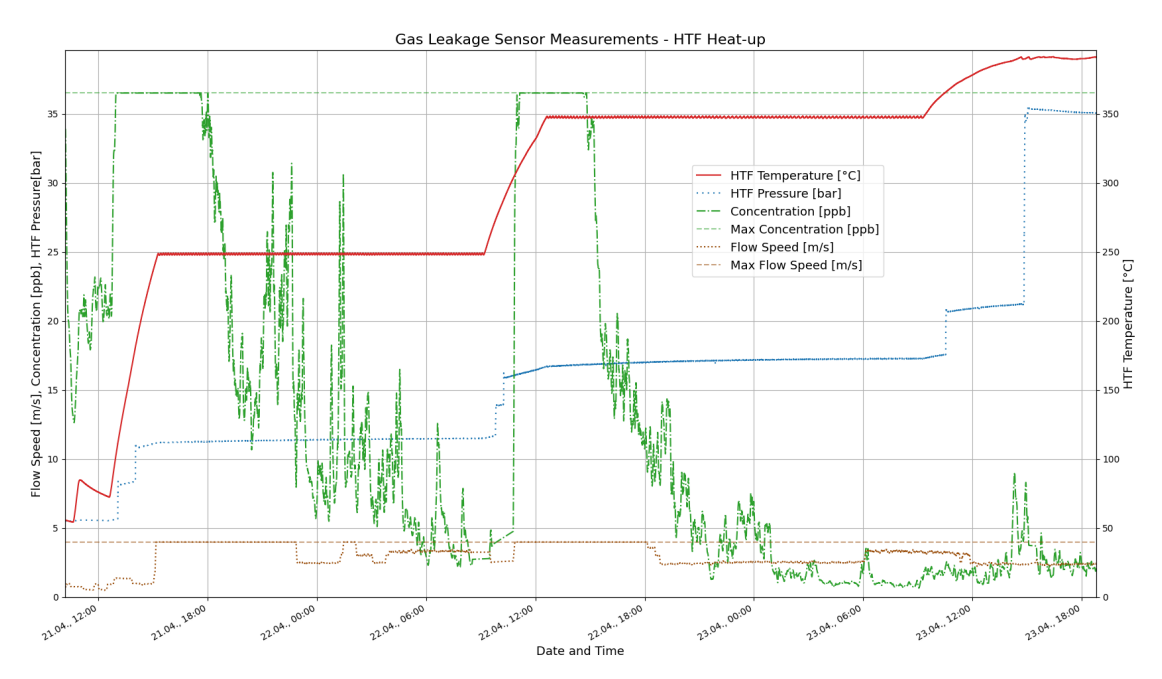


Figure 24: Gas concentration, airflow speed, and HTF temperature over time. The concentration and flow speed are reaching the sensors maximum values during and after heating.

The test rig experiment cycles start after heat-up is complete and the HTF temperature and pressure have stabilized. The measured gas concentration and airflow speed during the cycling phase are shown in Figure 25. Since the concentration remains low, the fan speed is not adjusted.

Figure 26 shows the measurements during the stable conditions after the power outage with the HTF kept at around 50 °C to 60 °C, 23 bar, and no movements before the

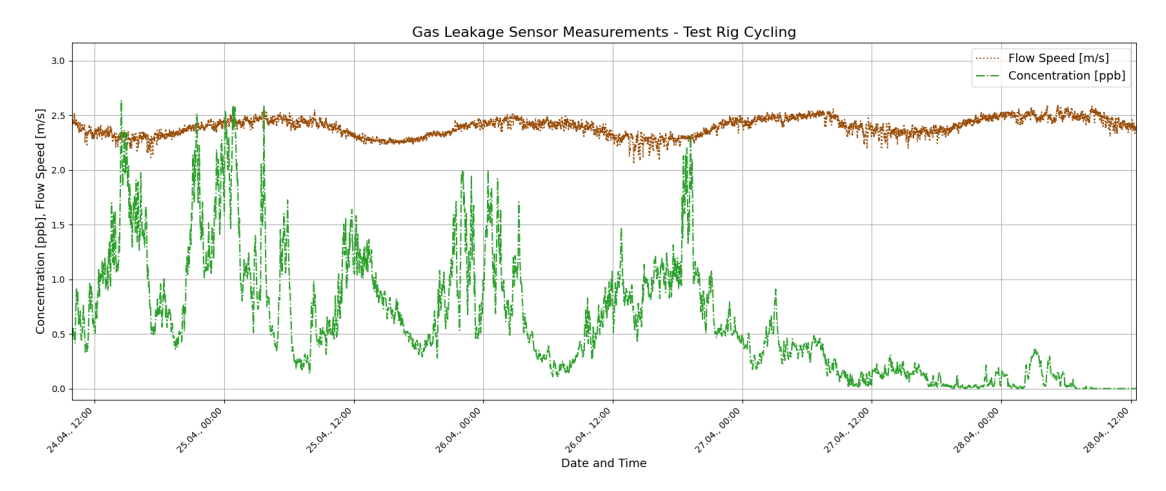


Figure 25: Gas concentration and airflow speed over time during the test rig cycling phase. The concentration remains low throughout.

experiment was taken on again. The gas concentration is increasing at nighttime to different extents, sometimes up to the maximum measuring range. This seems to relate to lower ambient temperature.

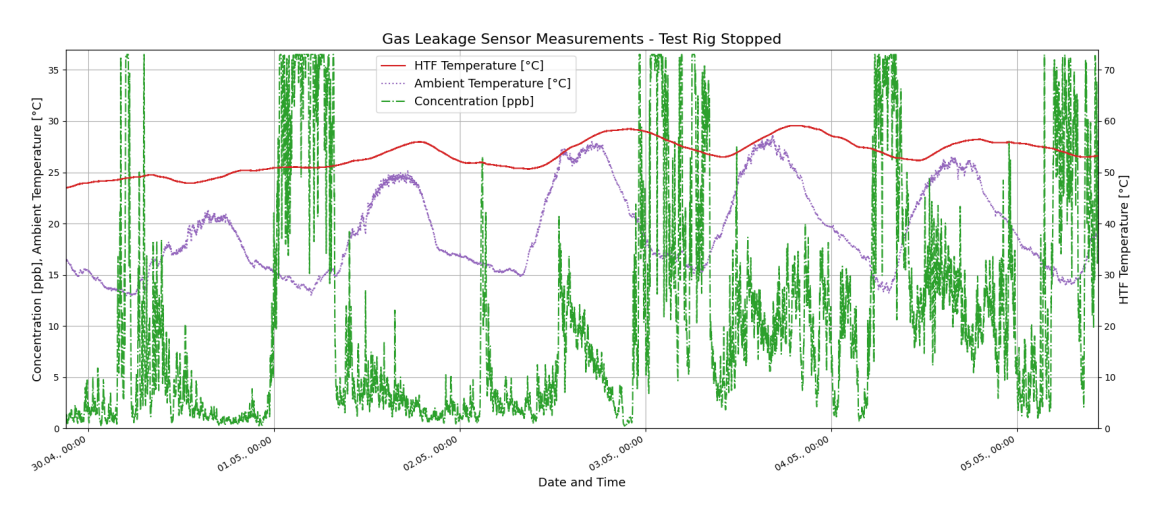


Figure 26: Gas concentration and ambient temperature over time at low HTF temperature, the test rig being stopped. The concentration is increasing every night, when the ambient temperature is lower.

5.2.2 HTF leakage analysis

Regarding the time series, several trends are observed that are hereafter investigated. The relationship between gas concentration and ambient temperature, number of completed cycles, HTF pressure, HTF temperature, and temperature evolution is analyzed. The data is also clustered by the experiment phases: cycling (relating to daytime in a CSP plant), transient phases (HTF heat-up and cool-down), and cold HTF temperature (relating to nighttime or stop of a CSP plant).

The correlation between the characteristic values and the gas concentration, segmented by experiment phase, is shown in Figure 27. The standard deviation of the concentration is also indicated for each segment. During transient phases, changes in HTF temperature and pressure exhibit the strongest influence on gas concentration, with HTF pressure showing a negative correlation. During the cycling phase, the standard deviation is relatively low, and the number of completed cycles shows the highest correlation, which is negative. At low HTF temperatures, the correlation of ambient temperature with gas concentration is weaker than that of HTF pressure and temperature. Across all phases, HTF pressure has the strongest influence on concentration. It should be noted that HTF temperature and pressure are interdependent due to the control of the HTF cycle.

Correlation with Concentration for the Experiment Phases All Data Std: 9.52 ppb Cycling Phase Std: 0.55 ppb Transient Phases HTF Temp < 70°C Std: 10.30 ppb Std: 11.11 ppb 1.00 Ambient Temperature -0.09 0.38 -0.10 0.36 0.50 HTF Pressure 0.30 -0.33 0.25 HTF Temperature -0.35 0.09 0.27 -0.30 0.00 -0.25HTF Temperature Change 0.33 0.11 0.12 -0.50 -0.75 Cycles completed 0.05 -0.05 -0.23

Figure 27: Correlation of experiment values on gas concentration, segmented by phase.

The standard deviation (std) of concentration values is given.

Gas concentration against ambient temperature is shown in Figure 28 for HTF temperatures below 70°C. Higher concentration values are observed only at low ambient temperatures, although the full range of concentrations is present.

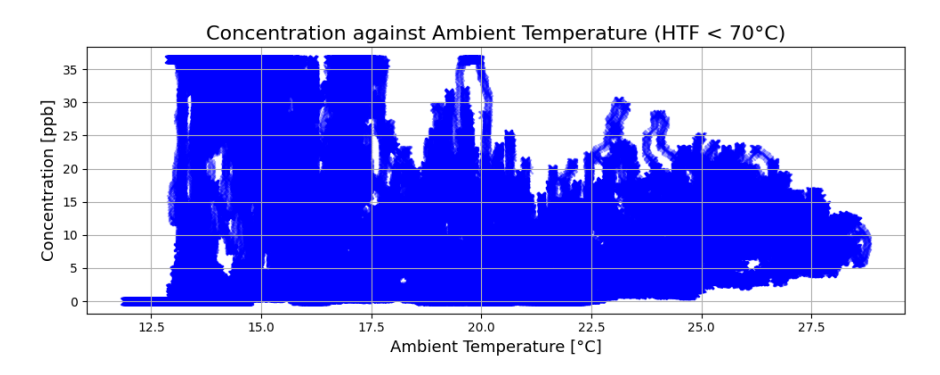


Figure 28: Gas concentration against ambient temperature for HTF colder than 70 °C.

Similarly, for transient phases with HTF temperatures above 70 °C and no cycling movement, gas concentration against HTF temperature change over three hours is shown in Figure 29. High concentrations are only observed at increasing HTF temperatures. During cool-down, the concentration values are low.

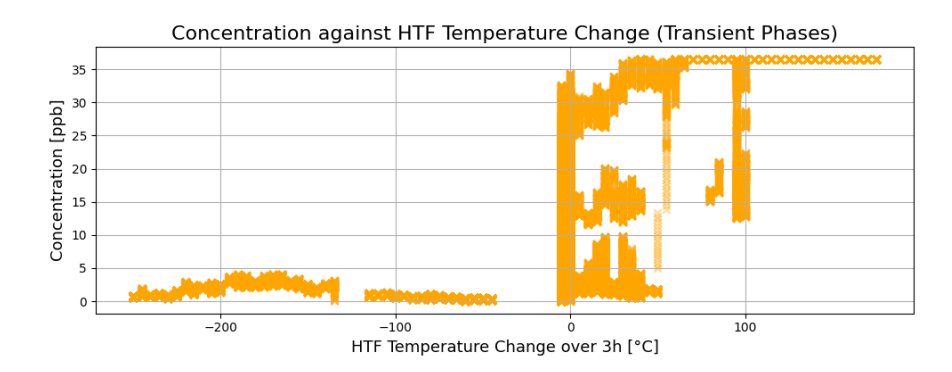


Figure 29: Gas concentration against HTF temperature change in three hours for HTF above 70 °C and no cycling.

This chapter reflects on the results obtained in the experiment phases. The BJAs were tested in the test rig, absolving rotational and translational movement in defined cycles, representing an accelerated lifetime testing. The objective is to determine the suitability of the installed cameras, the laser distance sensor, and the HTF leakage sensor for condition monitoring. In this chapter, the sensor setup, the data generated throughout the experiment phases, its evaluation, and the results are discussed. Additionally, further steps and optimization possibilities are developed.

6.1 Measurement setup and results

The measurement setup for the different observation methods and the results for each method separately and combining these are discussed here for the HTF leakage sensor as well as the geometric transformation observation with the cameras and the laser distance sensor. The angle which is formed by the two tubes connecting the three ball joints is observed to determine whether changes in the mechanical geometry occur over the performed cycles.

6.1.1 Cameras

Three cameras observe the two BJAs installed at the test rig from different perspectives. Images are captured at predefined rotation angles in every fifth cycle. Squared ArUco

markers with a side length of 80 mm are attached to the REPA tubes, they are detected in the further processing of the images. The distance to and resolution of the cameras varies by perspective, so that also the size of the markers in the images appear different.

In general, the markers are well-detected whenever the lighting situation is good. Lights installed at the test rig for nighttime vision shine into some of the cameras and the images of these hours cannot be processed. The size of the markers is overall big enough for the detection and determination of their unique ID.

An analysis based on the pixel position of the detected ArUco markers is not feasible. This is due to the storing process of the images leading to delays so that the exact moment of capture is not corresponding to the predefined rotation angle for each cycle. A comparison of the marker coordinates in the image over time would show changes, reflecting the different rotation position and not necessarily a change of the tube angles, which is the value of interest.

The precision of the markers position detection is investigated with a non-moving marker seen by one of the cameras. The variance per corner typically ranges from zero to two pixels, with a maximum of up to four pixels. This precision is better than expected, given the small size of the marker in the image.

Detection inaccuracies lead to a significant change in the estimated real-world position of a marker. The influence on position change depends only partly on the amount of pixel detection shift, but also on the camera resolution and appearing marker size. The markers closest to one of the cameras have the lowest average 3D position variation per pixel detection shift. Cameras with higher resolution, larger markers, or those installed closer to the camera result in larger pixel size in the image. The proportion between a corner detected at a slightly moved pixel position and the total size of the marker is lower. Due to the high influence on the estimated 3D position, only the images of the camera closest to the test rig are evaluated. This camera does not observe a fixed marker, so that the effect of the marker pixel size on the detection precision cannot be checked.

In an optimized setup, the cameras should be installed closer to the test rig, have higher resolution, or the markers be larger. The influence of small pixel detection variation on the estimated 3D position of the markers would decrease and the further angle calculation better reflect the reality. It should also be tested whether installing the cameras at an angle to the setup, rather than straight on, has an influence on pose estimation along the Z-axis.

To investigate whether angle variations reflect actual geometric transformations of the tubes or are measurement noise from the detection process, two line fits were applied. By removing the most outlying marker, the influence of a marker's estimated position on the resulting line angle can be seen. The greater the distance of a marker from the line, the larger the change in the angle, which supports the practice of excluding the farthest outlying marker from the line fit. Overall, the influence of estimated position on the angle is small, particularly for the tube with markers closer to the camera. Differences in the average and maximum distances of markers to the line fits, as well as the impact of marker position on the angle, vary between the projections onto the XY and YZ planes, generally being greater for the latter. This finding supports the idea of adjusting the cameras' positioning at an angle to the test rig to assess its effect.

It can be concluded that angle variation might result partly from noise, but reflects also actual angle change. Additionally, all data for the line fit based on the three closest markers are removed if any of these have a distance greater than the threshold of 3 mm. As expected, most filtering is done for night time images, while at daytime only few cycles need to be filtered, showing that detection accuracy is overall good. The resulting tube angle data can be assumed to represent the actual geometric setup of the REPAs with high accuracy.

No long-term trend is observed for the tube angles. It can be concluded that in the installed REPA setup, the three ball joints offer many degrees of freedom and the angles vary slightly from one cycle to the other. This angle change does not show a clear indication for a necessary maintenance or failure of the ball joints in the completed 2,700

cycles, reflecting approximately seven years of operation. Although outgassing of HTF was observed after these cycles during reheating of the facility, indicating the need of maintenance, the exact moment is not known and no relation to the measured angles can be drawn. It could only be guessed whether one of the few outlying tube angles observed indicate an upcoming failure. Further continuation of the experiment could show whether a trend appears in a longer simulated lifetime. Failures would allow to correlate their moment of appearance to the tube angles.

In general, the observation by cameras and further image processing is concluded to be a feasible method to observe the structure for geometrical changes. The feasibility depends on the quality of the images, where lighting has a big influence. The accuracy depends mostly on the size of the markers in the image in pixels. No definitive conclusion can be drawn on whether the tube angles are reliable indicators for condition monitoring of BJAs, although in this experiment, the tube angles did not indicate an upcoming need for maintenance. On the other hand, no absolute failure of the BJAs occurred, which might have been preceded by detectable changes in tube angles.

6.1.2 Laser distance sensor

No data could be obtained from the laser distance sensor during the first experimental period, where 2,700 cycles were completed. Due to ongoing outgassing of the ball joints following maintenance, only 40 cycles were completed in the subsequent period, limiting the available laser measurements. Consequently, this work is restricted to analyzing data from this short time frame, corresponding to 40 operating days in a plant. To identify long-term trends and evaluate the suitability of distance measurements as a condition monitoring method, a longer operational period would be required.

The distance values of the eastern REPA target show a plausible behavior over the 40 cycles. The filtered values have a high precision. Long-term trends in the distance could show geometric transformation of the REPA. Issues in the measurement and storing setup

don't allow for further analysis of the test rig rotation angle values at the target edges and of the western REPA. One reason for the issues could be difficulties in detecting the edges. To avoid scattering of the light beam, a paper tape has been applied to the targets which produces a slightly round edge at the initially flat metal plate. Furthermore, slow processing of the conditions for detection and recording of the rotation value in the same moment might also lead to unclear values.

A thorough investigation of the mentioned and other possible issues with the distance measurement would be needed to be carried out to make use of this method. The accuracy of laser sensors and the easy data processing in comparison with the camera observation make the distance measurement a promising method. On the other hand, the setup and details for the correct detection of the targets lead to difficulties. The idea of reading four different values (position change of two REPA tubes in two directions each) with only one sensor increases the complexity: overlay of the targets needs to be avoided and specific calibration of the setup to the need of each target separately is not possible.

6.1.3 Camera and laser combined

The laser sensor measurements are taken at lower test rig rotation angles than the images. The data cannot be compared directly as the REPA tubes are in different positions depending on the rotation angle. The laser is measuring distances to the REPAs, which allow to conclude for geometric transformation. Only the angle of the lower tubes could be derived from these measurements, knowing the geometry of the setup. A comparison of trends observed through the image processing and the laser sensor can be done in long-term experiments. Overlaying the data of the two observation principles helps to verify their accuracy, but cannot be done in this work due to the limited available laser sensor data.

6.1.4 Further ideas for observation

To further improve the observation of the geometric setup, other than the mentioned issues and solutions, more ideas are developed in this section. Gravity sensors attached to each tube in a REPA could get accurate measurements of their angle over time and allow for easy data processing. One sensor per tube would be needed and they have to withstand the high temperatures of the tubes. Installation on the outside of the insulation could be feasible if the insulation itself is strongly fixed to the tubes and doesn't move due to temperature differences. Recording the angle data for the REPA tubes over time would directly show the desired value with estimated minimal need for data refinement and filtering. The method would be independent of the test rig's lighting conditions and unaffected by detection accuracy.

Additionally, 3D cameras could be used to observe the REPAs at the test rig and directly identify the positions of the tubes and ball joints. This approach would eliminate the need for pose estimation through marker detection, coordinate transformation, and angle calculation, thereby reducing noise in the measurements. As a result, geometrical transformations over time caused by cycling could be determined more accurately.

6.1.5 HTF leakage sensor

A HTF leakage measurement system, consisting of a gas concentration, a flow speed, and further sensors, and a fan to control the air flow through the measurement pipe, are placed near one of the ball joints of the eastern REPA. Due to mechanical constraints and the movements of the test rig, installation of an enclosure around the ball joint to capture all escaping gases and channel them into the measurement pipe was not feasible. This would be necessary to avoid influence of wind on the concentration values, as with the current setup, not all HTF gas is reaching the sensor. This is even more the case as an insulation is placed around the ball joint, which retains exiting HTF and acts as a barrier between the ball joint and the pipe entrance. All measured concentration

values are therefore of unknown uncertainty. However, observed smell near the test rig and visible outgassing especially during heat-up confirm the high concentration values measured in these phases.

Several times during the experiment, the gas concentration and the flow speed sensor reached their maximum measuring range, and the fan operated at maximum speed, resulting in undefined measurement values. Especially in the heat-up phase, the gas concentration cannot be determined.

The gas concentration remained consistently low throughout the cycling phase, indicating almost no measurable HTF leakage during operation. The analysis reveals a strong inverse correlation between gas concentration and the number of completed cycles. However, due to the very low standard deviation of concentration values in this phase, this correlation may not represent an actual trend. To obtain more meaningful data, the cycling phase should be extended to allow greater variation in concentration values over a longer experimental period. Additionally, controlling the fan speed in smaller increments at low airflow rates would help increase the range of gas concentration values within the sensor's measurement range.

During transient phases such as heat-up and cool-down, HTF pressure and changes in HTF temperature exhibit the strongest correlation with gas concentration. Both parameters are externally controlled according to a specified procedure, with pressure increasing alongside temperature. The time graph shows a clearer trend of decreasing gas concentration approximately three hours after heating stops, suggesting that the HTF temperature has the greater influence on gas concentration than pressure.

An increase in gas concentration at low ambient temperatures during the maintenance phase, when HTF temperature was low, is observed in the time plot but not represented in the correlation analysis. Although HTF temperature and pressure show the highest correlation in this phase, both remain nearly constant. In contrast, the concentration varies significantly at lower ambient temperatures, which may reduce the reliability of the correlation analysis due to the range of measured values. This is also reflected in the

plot of gas concentration versus ambient temperature, where high concentrations occur only at low temperatures, but alongside low concentration values.

The high gas concentration observed during HTF heat-up, when the tubes, ball joints, and sealing materials also experience temperature increases, is assumed to be related to increased movement and settling of the mechanical components. Different materials heat up at different rates, which may cause expansion at different times and lead to reduced sealing performance, resulting in leakage. A similar effect could cause the higher gas concentration at low ambient temperatures. Modeling the ball joints and their materials could help verify this assumption.

To determine the mass flow of leaking HTF, the setup records the necessary parameters. However, all evaporated fluid would need to be collected. Additionally, the correlation factor between the sensor response and the actual concentration of VP-1 (used here as HTF) is unknown within the sensor's measuring range and would need to be determined through laboratory calibration. Furthermore, to obtain meaningful data, the sensors must operate within their measurement limits. Due to these constraints, the mass flow is not calculated in this study.

6.1.6 Improved setup ideas

To improve the HTF leakage measurement in future experiments, several ideas are proposed to develop the setup and sensors specifically for the test rig's conditions. This initial test provided insights into the gas concentration values at the test rig. The limitations of the gas concentration and flow speed sensors, as well as the fan, need to be addressed. Ideally, a concentration sensor adapted for the used HTF with a wider measurement range would be implemented. Although a market research was conducted before developing the current sensor setup and no better options were found, there might be new alternatives offered. Otherwise, the fan should be replaced with a model capable of operating over a wider speed range, enabling the Sens-It sensor to remain within

its measurement range during heat-up and providing better resolution of concentration changes during the cycling phase. Consequently, the flow speed sensor would also need to be adapted if mass flow calculations are to be made. Most importantly, enclosing the ball joint in a sealed box to capture all escaping HTF gas and channel it into the sensor setup is essential for precise measurements. Additionally, the ball joint should not be insulated to allow for a direct sensor response, which would improve observation.

Currently, only one ball joint is observed. Installing multiple HTF leakage sensors could reveal differences among the BJA and increase the amount of data available for evaluation. If only one ball joint fails, the variation in measurements from the three ball joints would provide valuable insights into the method's suitability. To reduce costs, a single measurement system could be installed at the test rig and connected sequentially to the encapsulated ball joints, with clean air flushing between measurements.

Due to the heat from the HTF warming the air around the tubes and ball joints, the plastic tube used in the measurement setup is not well-suited. Replacing it with a metal tube can prevent deformation or melting, which not only poses a risk to the setup but could also cause material evaporation that may affect the measurements. For further use of the HTF leakage sensor in operating CSP plants, the setup could be made transportable and independent from a power source by adding a battery and solar panel.

On the data evaluation side, a machine learning algorithm could identify patterns of the concentration values during transient and cycling phases. Deviations from these pattern during operation could indicate an upcoming failure or the need of maintenance.

6.1.7 Combining results from the methods

Angle changes observed by the cameras and laser sensor can only occur during movement of the REPAs. The HTF leakage concentration remained low throughout the corresponding cycling phase. It is possible that the upcoming need for maintenance is not reflected in either the tube angles or the gas concentration. A longer experiment including a ball

joint failure could reveal whether higher concentration values, angle changes, or both occur prior to failure. While a correlation might exist, it cannot yet be confirmed.

6.2 Use in a CSP Plant

The test rig differs from a CSP plant in several ways. The rotation speed of the test rig, which represents the tracking mechanism in a plant, is higher. The slower, incremental movements of a PTC may lead to leakages and gas concentration patterns different from those observed in the test rig. Additionally, the highest gas concentrations were measured during heat-up, happening daily in a CSP plant. Given these differences in motion and further environmental factors, testing the implemented methods on an actual CSP plant could provide further insights into their suitability for condition monitoring.

While it is possible to install the implemented methods on REPAs within a CSP plant, monitoring an entire plant would require extensive effort due to the large number of REPAs installed. An alternative approach could involve using mobile sensors and cameras that circulate throughout the PTC field, performing occasional measurements. Reference positions fixed on the PTC structures for the cameras and laser sensors would facilitate the application of these methods in CSP plants.

7 Summary and Outlook

This work integrates three cameras, a laser distance sensor, and a HTF leakage sensor into a REPA test rig. Their suitability for condition monitoring of BJAs is evaluated based on data collected during an experiment. PTCs are the most commonly used type of electricity-producing CSP, where HTF temperatures reach up to 400 °C and pressures up to 35 bar by concentrating solar rays on a receiver tube. REPAs must accommodate both rotational and translational movements in a PTC due to sun tracking and thermal expansion of the receiver tubes. Condition monitoring aims to anticipate maintenance needs or failures that could lead to contamination or fires.

The test rig at PSA features two BJA-type REPAs, each with three ball joints and two connecting tubes. The experiment consists of several stages: a heat-up phase, a cycling phase of 2,700 cycles (representing an accelerated lifetime of roughly seven years of operation), and a maintenance phase. Strong outgassing of evaporated HTF was observed after the cycling, indicating the need for maintenance.

Three cameras capture images at predefined rotation angles during cycling. ArUco markers are attached to the BJA tubes, detected by a processing software, and their positions estimated in 3D space. Detection precision is high with minimal noise, however, 3D position estimates are sensitive to noise, especially for smaller appearing markers. Only images from the camera closest to the test rig were suitable for evaluation, as the markers appear larger in the images and noise influence is acceptable. Lines are fitted through the estimated marker positions to reconstruct the tubes and calculate the angle between them. After filtering, angle accuracy is about 0.5° and reflects actual tube movement.

7 Summary and Outlook

Although small angle variation occurs from cycle to cycle, no long-term trend is apparent. Therefore, it remains inconclusive whether angle changes are reliable indicators for condition monitoring, and extended experiments could reveal trends.

A laser distance sensor is installed next to the test rig, measuring distances to targets on the lower BJA tubes. Changes in these distances would also indicate geometrical transformations. However, data gaps during the cycling phase and the complex setup prevent conclusions within the scope of this work. With an improved setup and data storage method, the laser sensor could deliver precise and accessible data.

To detect HTF leakage, a sensor setup along a plastic tube records gas concentration, ambient temperature, and airflow speed. The highest gas concentration occurs during heat-up, reaching the sensor's maximum range of 36.5 ppb. Concentration remains low throughout cycling, with no observable trend indicating increased leakage from ball joint wear. Several improvements to the sensor setup and installation are proposed to refine measurements.

Future work should implement the improvements discussed in Chapter 6, continue analyzing data from further experiments, and evaluate any emerging trends. Data collected prior to an actual failure event could reveal deviations from the current values, potentially indicating upcoming failure and demonstrating the suitability of one or more methods. While each of the three methods can be implemented for REPA condition monitoring, their effectiveness has not yet been fully proven. Deploying these methods in a real PTC plant would provide valuable insights into their practical applicability and reliability for condition monitoring.

Bibliography

- [1] Grand View Research, Concentrated solar power market size, share & trends analysis report by technology (parabolic trough, linear fresnel, dish, power tower), by application, by region, and segment forecasts, 2025–2030, 2024.
- [2] A. Fernández-García, E. Zarza, L. Valenzuela, and M. Pérez, "Parabolic-trough solar collectors and their applications," Renewable and Sustainable Energy Reviews, vol. 14, no. 7, pp. 1695–1721, 2010, ISSN: 1364-0321. DOI: 10.1016/j.rser.2010.03.012.
- [3] CIEMAT. "Plataforma solar de almeria objectives," Accessed: Mar. 26, 2025. [Online]. Available: https://www.psa.es/en/gen/objetivos.php.
- [4] A. H. Alami et al., "Concentrating solar power (csp) technologies: Status and analysis," *International Journal of Thermofluids*, vol. 18, p. 100340, 2023, ISSN: 2666-2027. DOI: https://doi.org/10.1016/j.ijft.2023.100340.
- [5] E. Mäki et al., "Concentrated solar power and circulating fluidized bed power plant hybrids final results of the combo-cfb project," VTT Technical Research Centre of Finland, Tech. Rep., Apr. 2017. DOI: 10.13140/RG.2.2.20145.58722.
- [6] L. A. Weinstein, J. Loomis, B. Bhatia, D. M. Bierman, E. N. Wang, and G. Chen, "Concentrating solar power," *Chemical Reviews*, vol. 115, no. 23, pp. 12797–12838, 2015, PMID: 26511904. DOI: 10.1021/acs.chemrev.5b00397.

Bibliography

- [7] H. Benoit, L. Spreafico, D. Gauthier, and G. Flamant, "Review of heat transfer fluids in tube-receivers used in concentrating solar thermal systems: Properties and heat transfer coefficients," Renewable and Sustainable Energy Reviews, vol. 55, pp. 298-315, 2016, ISSN: 1364-0321. DOI: https://doi.org/10.1016/j.rser. 2015.10.059. [Online]. Available: https://www.sciencedirect.com/science/article/pii/S1364032115011387.
- [8] Y. Krishna, M. Faizal, R. Saidur, K. Ng, and N. Aslfattahi, "State-of-the-art heat transfer fluids for parabolic trough collector," *International Journal of Heat and Mass Transfer*, vol. 152, p. 119541, 2020, ISSN: 0017-9310. DOI: 10.1016/j.ijheatmasstransfer.2020.119541.
- [9] Duratherm. "Duratherm s." Accessed: 2025-07-10, Duratherm. [Online]. Available: https://durathermole.de/produkte/duratherm-s.
- [10] T. Müller, "Commissioning and validation of the underlying model of a test rig analyzing rotation and expansion performing assemblies in parabolic trough collector power plants," Master's thesis, RWTH Aachen Institute of Solar Research, German Aerospace Center (DLR), 2017.
- [11] H. Tobias, "Design of the motion control for a test rig analyzing rotation and expansion performing assemblies in parabolic trough collector power plant applications," Hochschule Mannheim University of Applied Sciences, German Aerospace Center (DLR), 2016.
- [12] S. Garrido-Jurado, R. Muñoz-Salinas, F. Madrid-Cuevas, and M. Marín-Jiménez, "Automatic generation and detection of highly reliable fiducial markers under occlusion," *Pattern Recognition*, vol. 47, no. 6, pp. 2280–2292, 2014, ISSN: 0031-3203. DOI: https://doi.org/10.1016/j.patcog.2014.01.005.
- [13] D. Brown, "Decentering distortion of lenses," 1966. [Online]. Available: https://api.semanticscholar.org/CorpusID:117271607.

Bibliography

- [14] OpenCV Developers. "Calib3d module documentation." Accessed: 2025-07-07, OpenCV. [Online]. Available: https://docs.opencv.org/4.x/d9/d0c/group_calib3d.html.
- [15] A. Monrroy Cano, J. Lambert, M. Edahiro, and S. Kato, "Single-shot intrinsic calibration for autonomous driving applications," Sensors, vol. 22, no. 5, 2022, ISSN: 1424-8220. DOI: 10.3390/s22052067. [Online]. Available: https://www.mdpi.com/1424-8220/22/5/2067.
- [16] B. Gábor. "Camera calibration." Accessed: 2025-06-12, OpenCV. [Online]. Available: https://docs.opencv.org/4.x/d4/d94/tutorial_camera_calibration.html.
- [17] OpenCV Developers. "Solvepnp pose estimation." Accessed: 2025-06-11, OpenCV. [Online]. Available: https://docs.opencv.org/4.x/d5/d1f/calib3d_solvePnP. html.
- [18] S. Garrido and A. Panov. "Opency: Detection of aruco markers." Accessed: 2025-06-11, OpenCV. [Online]. Available: https://docs.opencv.org/4.x/d5/dae/tutorial_aruco_detection.html.
- [19] Suh and Y. Soo, "Laser sensors for displacement, distance and position," Sensors, vol. 19, no. 8, 2019, ISSN: 1424-8220. DOI: 10.3390/s19081924.
- [20] M. Hardelt, "Development of a measurement method for continuous quantification of heat transfer fluid vapor in air," Master's thesis, DLR Institut für Solarforschung Köln/Almería, 2023.
- [21] United S.r.l. "Sens-it datasheet," Accessed: Jun. 4, 2025. [Online]. Available: http://www.united-srl.com/site/wp-content/uploads/2015/04/SENS-IT-Datasheet.pdf.